JGR Space Physics

Key Points:
- Counterstreaming ion beams observed by THEMIS confirm two reconnection X-lines around a nascent FTE flux rope in agreement with a PIC simulation
- THEMIS observed tripolar out-of-plane (B_M) magnetic fields across a nascent flux rope and a mature FTE flux rope
- PIC simulations suggest that a tripolar B_M at a nascent flux rope is due to unipolar Hall magnetic fields from two X-lines at an asymmetric current sheet

Correspondence to:
S. Eriksson,
eriksson@lasp.colorado.edu

Nascent Flux Rope Observations at Earth's Dayside Magnetopause

S. Eriksson[1] (iD), **V. M. Souza[2,3]** (iD), **P. A. Cassak[3]** (iD), and **S. Hoilijoki[1]** (iD)

[1]Laboratory for Atmospheric and Space Physics, University of Colorado Boulder, Boulder, CO, USA, [2]National Institute for Space Research/INPE, São José dos Campos, SP, Brazil, [3]Department of Physics and Astronomy, West Virginia University, Morgantown, WV, USA

Abstract Two THEMIS satellites, separated by only 0.38 Earth radii (R_E), traversed two consecutive dayside magnetopause (MP) current sheets at $3.5 < Z_{GSM} < 3.8 R_E$ on 15 November 2010. An early-stage crater-like flux transfer event (FTE) with weakly enhanced total pressure is sampled at the first, complete outbound MP crossing. A mature FTE flux rope is observed just 70 s later across the second, inbound crossing of the MP current sheet. Two counterstreaming magnetosheath ion beams at the interface of two converging reconnection exhausts earthward of the MP current sheet provide direct evidence of two X-lines across the early-stage crater FTE. A D-shaped ion beam observed along the southward magnetic field in the magnetosheath boundary layer and northward exhausts observed earthward of the MP provide evidence of two X-lines across the mature FTE flux rope. Tripolar out-of-plane magnetic field perturbations (ΔB_M) of substantial magnitudes were sampled across the MP current sheet in both stages of the FTE flux rope evolution. These dayside observations suggest an association between a tripolar ΔB_M perturbation with two magnetic reconnection X-lines and FTE flux rope formation. A dedicated particle-in-cell numerical simulation of magnetic reconnection reproduces similar ion velocity distributions and out-of-plane magnetic field perturbations at an asymmetric current sheet as those observed across a nascent flux rope between two X-lines at the dayside asymmetric MP.

1. Introduction

The physical origin of the magnetic field structures referred to as flux transfer events (FTEs) has remained elusive ever since their first observation at the dayside magnetopause (MP) was reported in the seminal papers by Russell and Elphic (1978, 1979). The FTE magnetic structure is often characterized as a helical flux rope in three dimensions (3-D) with a substantial axial (core) magnetic field. The moving FTE produces a strong bipolar variation of the MP normal component (B_N) of the magnetic field in a boundary normal LMN coordinate system as the structure propagates along the MP surface. Here, **L** is the direction of maximum variation of the magnetic field (e.g., Sonnerup & Scheible, 1998) across the MP current sheet, **N** is the outward normal direction, and **M** = **N** × **L** completes a right-handed LMN coordinate system.

Daly et al. (1981) reported that the FTE center region is associated with mixed plasma populations with origins in both the magnetosphere and the magnetosheath. This means that magnetic field reconnection (e.g., Birn et al., 2001; Dungey, 1961) is required at some point in the formation of FTEs to allow plasmas from the two regions to mix across the MP current sheet. Southwood et al. (1986) and Scholer (1988) proposed that a nonsteady, bursty magnetic reconnection process would result in a temporary bulge of plasma propagating away from a single X-line in the subsolar MP region. In a competing scenario, Lee and Fu (1985) suggested that the simultaneous presence of multiple X-lines at the MP current sheet could explain the origin of FTEs, such that a helical magnetic flux rope would form in between a pair of X-lines. Raeder (2006) suggested that FTEs form via multiple, sequentially active reconnection X-lines (MSXR) based on 3-D magnetohydrodynamic (MHD) simulations of Earth's magnetosphere with a dipole tilt. The MSXR scenario envisions that one single X-line forms in a preferred dayside MP location. The external forcing of the magnetosheath flow then causes this first X-line to drift away from the primary X-line source region. A second X-line is proposed to form in the wake of the first X-line under assumptions of relatively steady external magnetic fields and plasma conditions. The 3-D MHD simulations reported by Raeder (2006) illustrate how a flux rope can grow in size and magnetic field strength between the two X-lines in general agreement with Lee and Fu (1985). This cycle could repeat itself with new X-lines and flux ropes forming semiregularly at the dayside MP.

Wang et al. (2005) examined Cluster satellite observations (Escoubet et al., 2001) at the high-latitude dayside MP and reported increased FTE occurrences in the local winter hemisphere in general agreement with the MSXR model. Hasegawa et al. (2010) presented some of the first observational evidence in favor of the MSXR scenario from string-of-pearl satellite observations of an FTE using the Time History of Events and Macroscale Interactions during Substorms (THEMIS) multispacecraft mission (Angelopoulos, 2008) during predominantly interplanetary magnetic field (IMF) $By > 0$ conditions in the adjacent magnetosheath. However, as noted by Dorelli and Bhattacharjee (2009), a dipole tilt is not a necessary condition to generate dayside FTE flux ropes. Other factors may also contribute to FTE flux rope formation and evolution, such as the IMF cone angle causing a north-south asymmetry of dayside FTE occurrence rates (Hoilijoki et al., 2019). In a numerical test case with zero dipole tilt angle and IMF $Bz < 0$, Hoilijoki et al. (2019) suggest that smaller and more frequent FTEs may be common in the Northern Hemisphere for a positive IMF Bx, while larger and less frequent FTEs are predicted in the Southern Hemisphere. Fuselier et al. (2018) suggested that large-scale multiple reconnection X-lines may be a common occurrence at the dayside MP during southward IMF Bz conditions on the basis of bidirectional streaming electrons and counterstreaming protons as measured along the local magnetic field by the Magnetospheric Multiscale (MMS) satellites.

Whether dayside magnetic field reconnection takes place predominantly at a single X-line, or to some extent via multiple X-lines, is a topic of great importance to understand FTE formation, MP structure, and the coupling between the solar wind and the magnetosphere. Magnetic reconnection generates a pair of plasma exhausts in opposite L directions from a central X-line (e.g., Birn et al., 2001, and references therein). Electrons typically stream along the magnetic field of each separatrix toward the X-line in the electron diffusion region (e.g., Burch et al., 2016), where they are ejected in two electron jets (e.g., Phan et al., 2007; Wilder et al., 2017) that merge with the ion jets of the downstream exhausts. The currents associated with this loop of field-aligned electron flow when projected on the NL plane of the reconnection X-line geometry correspond to the in-plane Hall currents that generate an out-of-plane B_M quadrupole Hall magnetic field near the X-line (e.g., Birn et al., 2001; Mandt et al., 1994; Sonnerup, 1979; Terasawa, 1983). The Hall magnetic fields, which may result in very large bipolar perturbations to the background out-of-plane (guide) magnetic field (B_G) across each reconnection exhaust, are antisymmetric when B_G is small and when the plasma density and magnetic field strength are nearly equal on both sides of the current sheet. Satellite observations through such symmetric exhausts at the dayside MP have confirmed a bipolar ΔB_M variation consistent with a quadrupole Hall magnetic field, where $\Delta B_M = B_M - B_G$ (e.g., Mozer et al., 2002). The quadrupole nature of the Hall magnetic fields changes considerably in the presence of finite B_G or strong gradients of the adjacent plasma density and magnetic field strength (e.g., Birn et al., 2008; Eriksson et al., 2014; Karimabadi et al., 1999; Pritchett, 2008; Pritchett & Mozer, 2009). Therefore, the out-of-plane ΔB_M variations provide excellent insight into the plasma parameters and magnetic environment of the reconnection region and consequently of FTE flux ropes.

Chen et al. (2017) presented some early-stage FTE evolution signatures between pairs of X-lines at the dayside MP current sheet in a global 3-D MHD simulation with an embedded particle-in-cell (PIC) code. This MHD-EPIC code (Daldorff et al., 2014; Tóth et al., 2017) captures the physics of multiple magnetic reconnection X-lines within the embedded PIC domain at the dayside MP. They reported that simulated FTEs in their early formation stages were associated with noticeable depressions of the core region magnetic field strength and thus reminiscent of "crater" FTEs (LaBelle et al., 1987; Owen et al., 2008; Sibeck et al., 2008; Zhang et al., 2010). The results of the MHD-EPIC simulation are consistent with the scenario that crater FTEs with weak core fields correspond to the early stages of FTE formation as first proposed by Zhang et al. (2010) from a large database of FTEs recorded by the THEMIS satellites. The simulated FTEs that Chen et al. (2017) examined obtained a typical flux rope structure once the core field region acquired a significant amount of axial magnetic flux. Interestingly, this growth of the axial core field transpired despite the absence of a background guide field ($B_G = 0$). It was suggested that a Hall magnetic field might evolve into a core field of the FTE, as first proposed by Karimabadi et al. (1999) to explain the core field generation of magnetotail plasmoids. Finally, Chen et al. (2017) also reported evidence of a tripolar ΔB_M perturbation of the out-of-plane magnetic field along a diagonal path through an early-stage crater FTE.

Eriksson et al. (2014, 2015) discovered the first in situ evidence of tripolar ΔB_M perturbations across solar wind reconnection exhausts (e.g., Gosling et al., 2005) in nearly symmetric external conditions. The

tripolar ΔB_M consists of a central B_M enhancement sandwiched between two B_M depressions $\Delta B_M < 0$. Eriksson et al. (2016) subsequently reported the first in situ observation of a tripolar ΔB_M magnetic field across Earth's subsolar MP current sheet from Polar satellite observations. The Polar observations were characterized by nearly symmetric conditions in both plasma density (Np) and magnetic field strength (B) across the subsolar MP. This tripolar ΔB_M signature was shown to be in good agreement with the magnetic field signatures of a magnetic island generated between two X-lines in a two-dimensional (2-D) PIC simulation for similarly symmetric conditions across the current layer.

The Polar satellite measurements could not ascertain whether one or multiple X-lines were present on either side of the proposed magnetic island at the subsolar MP when a tripolar ΔB_M perturbation was observed on a background guide field $B_G/B_L = 0.3$ (Eriksson et al., 2016). However, the three THEMIS satellites with a 12 R_E orbit apogee (1 $R_E = 6{,}378.137$ km) frequently traversed the dayside MP at $|Y_{GSM}| < 3\,R_E$ in October–December of 2010 and 2011 with a separation $\Delta R < 2\,R_E$ between any two satellites in a geocentric solar magnetospheric (GSM) coordinate system (e.g., Hapgood, 1992). This configuration of multisatellite observations can be used to explore FTE flux rope formation and, specifically, to address the question of whether multiple X-lines generate tripolar ΔB_M perturbations at the dayside MP. Here, we present observations recorded by the THEMIS-A (TH-A) and THEMIS-E (TH-E) satellites in an optimal spatial configuration across two consecutive traversals of an asymmetric dayside MP on 15 November 2010 that we associate with flux rope signatures. In section 2, we first present an overview of the THEMIS observations in GSM coordinates north of the dayside equator and their comparisons with the solar wind conditions as recorded by the Advanced Composition Explorer (ACE) satellite in the upstream solar wind (e.g., Stone et al., 1998). We then examine these THEMIS observations of substantial tripolar ΔB_M perturbations to the guide magnetic field in a local boundary normal LMN coordinate system of the two MP current sheets. Section 2 also reports a number of ion velocity distribution functions (VDFs) that TH-A and TH-E measured across both MP crossings. We confirm a presence of counterstreaming ion beams around the FTE flux ropes as supporting evidence for the presence of two reconnection X-lines near the satellites. Section 3 summarizes the THEMIS observations of the two MP crossings using a schematic representation of proposed magnetic islands in two different stages of evolution. In section 4, we present the results from a dedicated 2-D PIC simulation of magnetic islands and multiple reconnection X-lines for the observed asymmetric parameters across the first, outbound MP crossing that we associate with a nascent flux rope. Section 4 also reports four simulated ion VDFs along an outbound, virtual satellite trajectory that compare favorably with those measured by THEMIS. We follow the evolution of representative ion particle trajectories from the simulated ion VDFs to understand their time history from the adjacent magnetosheath into the MP boundary layer. Section 5 provides a dedicated discussion of the key results obtained in this event study of observations and simulated signatures across an early stage flux rope at the dayside MP. In section 6, we provide a summary and conclusion of this comparative analysis of the observed and simulated ion-scale signatures across a nascent flux rope that shed new light on the association between tripolar ΔB_M signatures, multiple reconnection X-lines, and the early core field evolution of FTE flux ropes at a dayside asymmetric MP current sheet.

2. THEMIS Observations and Upstream Solar Wind Conditions

NASA launched the five identical THEMIS satellites into a near-equatorial orbit on 17 February 2007. Two THEMIS satellites, TH-B and TH-C, were later maneuvered toward their Lunar ARTEMIS mission orbit with TH-B arriving at a nearside Lissajous orbit on 1 September 2010. TH-C arrived into its farside Lissajous orbit on 19 October 2010. The present study explores THEMIS observations across two consecutive dayside MP crossings during the 2117–2122 UT period on 15 November 2010 by TH-A, TH-D, and TH-E. We take advantage of measurements recorded by the ion Electro-Static Analyzer (ESA) instrument at 3 s spin resolution (McFadden et al., 2008) and 0.25 s cadence magnetic field observations by the fluxgate magnetometer (FGM) instrument (Auster et al., 2008).

2.1. Observations in GSM Coordinates

Figure 1 shows the GSM positions of all three THEMIS satellites (TH-A, TH-D, and TH-E) on 15 November 2010 at 2119:00 UT when TH-A moved into the magnetosheath across the first MP boundary layer with TH-A located at $[X_{GSM}, Y_{GSM}, Z_{GSM}] = [10.114, -0.827, 3.803]\ R_E$, TH-D at $[10.275, -0.252, 3.672]\ R_E$, and TH-E at $[10.300, -0.614, 3.546]\ R_E$. That is, TH-A is the northernmost satellite with a
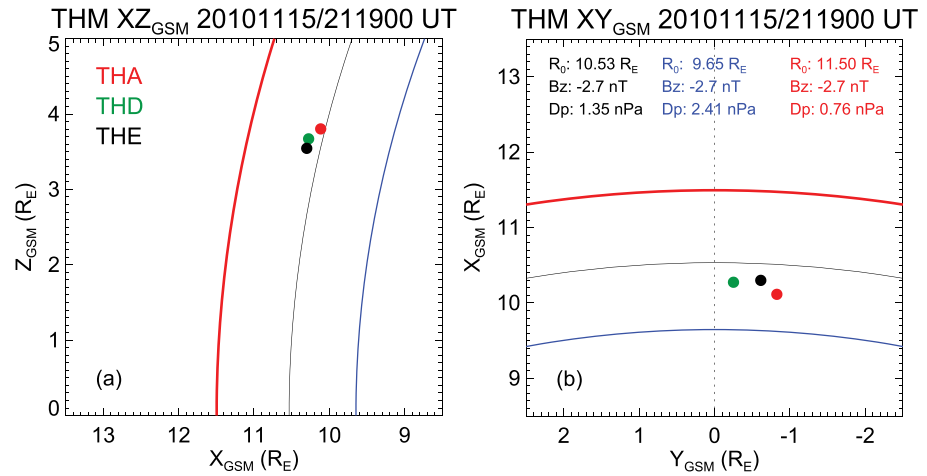
Figure 1. THEMIS (A, D, E) GSM positions at the 2119:00 UT time of a magnetopause (MP) crossing on 15 November 2010. Three modeled magnetopause surfaces are shown for the same average IMF $Bz = -2.7$ nT and three proposed values of the upstream solar wind dynamic pressure (Dp) as input to the Shue et al. (1997) MP model around this outbound MP crossing. TH-A is located at $[10.1144, -0.827036, 3.80347]$ R_E, TH-D is located at $[10.2745, -0.251858, 3.67159]$ R_E, and TH-E is located at $[10.2996, -0.613929, 3.54551]$ R_E. Here, 1 $R_E = 6,378.137$ km.

$\Delta Z_{GSM} = 0.257$ R_E separation from the southernmost TH-E satellite. TH-E was only separated by $\Delta Y_{GSM} = 0.213$ R_E from TH-A, while TH-D was separated by another $\Delta Y_{GSM} = 0.362$ R_E from TH-E. Figure 1 also illustrates three alternative MP surface locations for global context at 2119:00 UT as we discuss later. The positive Z_{GSM} location of THEMIS on 15 November 2010 increases the likelihood that it will detect northward moving MP structures from a subsolar source region.

A detailed analysis of magnetic field structures believed to be generated at the dayside MP current sheet, such as flux ropes, requires a knowledge of the upstream magnetic field to confirm whether the structures are embedded in the solar wind or associated with the local MP. None of the three THEMIS satellites could provide these external conditions due to the small satellite separations. Here, we use upstream solar wind observations from the ACE satellite, OMNI data (King & Papitashvili, 2005) and TH-C observations sampled in the magnetosheath at $[X_{GSM}, Y_{GSM}, Z_{GSM}] = [-32.9, 47.6, 1.9]$ R_E to constrain a time delay of the ACE data to the dayside MP. Figure 2 compares a 30 min overview of time-shifted ACE observations (1 s IMF magnetic fields and 64 s plasma measurements) with 1 min OMNI magnetic fields and TH-A observations at 2057–2127 UT. ACE is the source satellite of the OMNI observations shown in Figures 2a–2c that we shifted forward in time by 1.8 min to account for an average plasma convection delay between the bow shock and the dayside MP. We translated the ACE observations forward in time by a constant 39.5 min time delay from the L1 point to the dayside MP in order for the high-cadence IMF to match the time-shifted OMNI magnetic field. We obtained the 1.8 min time correction of the OMNI data under assumptions of a constant dayside magnetosheath flow speed $V_{MS} = 161.5$ km/s along plasma streamlines with an average 2.83 R_E separation between a bow shock location X_{BS} and a subsolar MP location X_{MP} for the 2115–2125 UT period on 15 November 2010. Figure 2f shows X_{BS}, provided by OMNI, as well as X_{MP}, which is estimated from ACE observations and the Shue et al. (1997) model. Here, $V_{MS} = 161.5$ km/s is obtained as the magnitude of the average ion velocity $\mathbf{V}i_{GSM} = [-137.3, 33.0, 78.4]$ km/s that TH-A measured in the adjacent magnetosheath (see Figures 2g–2i) between 2119:09 and 2119:28 UT.

This report focuses on THEMIS observations of two consecutive MP encounters. TH-A exited the first MP current sheet layer at 2119:00 UT, and it reentered a subsequent MP layer at 2120:10 UT after a short period in the adjacent magnetosheath. Figures 2a–2c suggests that the first MP observations occurred less than 1–2 min after the IMF turned southward ($Bz < 0$) and dawnward ($By < 0$) at ~2117–2118 UT after a ~10 min period of northward IMF $Bz > 0$ and duskward IMF $By > 0$. TH-C observed the same southward Bz rotation at 2126:26 UT in the magnetosheath well beyond the terminator (not shown) after an extended period when the Bx component had remained stable with a large positive value. ACE originally observed this same
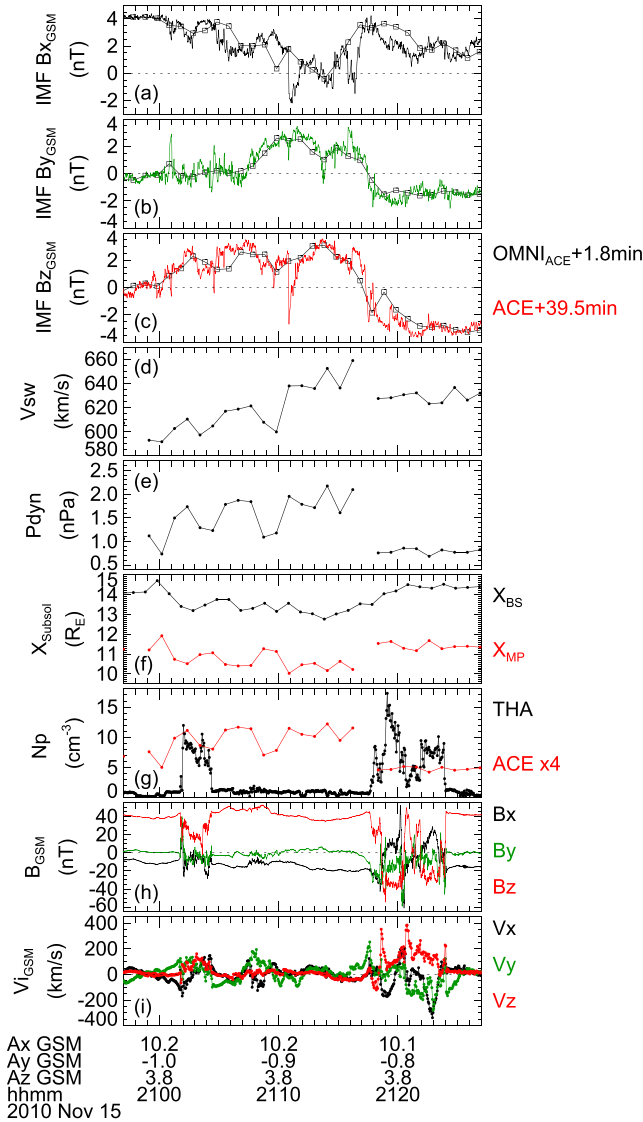
Figure 2. (a–e) ACE observations (1 s IMF and 64 s SWEPAM) shifted forward in time by 39.5 min from the L1 point to the dayside magnetopause at 2057–2127 UT on 15 November 2010. OMNI 1 min IMF data (source: ACE) are shifted forward in time by 1.8 min through the magnetosheath (symbols in Panels a–c) on the basis of TH-A velocity observations in the magnetosheath at 2119:09–2119:28 UT; (f) predicted subsolar locations of the bow shock (black) and magnetopause (red) in terms of Earth radii; (g) plasma number density (N_p) as observed by TH-A (black) and a shocked solar wind density $N_\mathrm{MS} = 4N_\mathrm{sw}$ as observed by ACE (red); (h) GSM magnetic field observed by TH-A; and (i) GSM ion velocity observed by TH-A.

southward IMF Bz rotation 48.6 min earlier at 2037:51 UT after a similarly stable period of positive IMF Bx. Although the TH-B satellite sampled a high-speed 593 km/s solar wind at $[X_\mathrm{GSM}, Y_\mathrm{GSM}, Z_\mathrm{GSM}] = [-22.4, 65.6, 0.1]$ R_E at this time and a similarly stable IMF Bx (not shown), it did not observe a subsequent southward rotation of the IMF Bz this far from the ACE observations and the Sun-Earth line. The 48.6 min delay from ACE to TH-C of the same Bz rotation and the proposed 39.5 min delay from ACE to TH-A at the dayside MP would suggest a 546 s propagation delay between TH-A at $X_\mathrm{GSM} = 10.1$ R_E and TH-C at $X_\mathrm{GSM} = -32.9$ R_E. This corresponds to a mean Vx $= -503$ km/s propagation speed through the magnetosheath in excellent agreement with the 15 min average Vx $= -501$ km/s speed that TH-C measured in the magnetosheath at 2121:27–2136:24 UT at the time of the southward Bz rotation. The estimated 1.8 min time delay from the bow shock to the dayside MP appears to be well constrained by these ACE, OMNI, and TH-C observations.

Figure 1 shows three possible dayside MP model locations for the same IMF Bz and three different values of the dynamic pressure $Dp = N_\mathrm{sw} m_\mathrm{p} V_\mathrm{sw}^2$ as input to the Shue et al. (1997) empirical MP model. Here, N_sw is the solar-wind plasma number density, V_sw is the solar wind speed, and $m_\mathrm{p} = 1.67 \cdot 10^{-27}$ kg is the proton rest mass. We obtained this IMF $Bz = -2.7$ nT as the 1 min average of the time-shifted 1 s cadence IMF Bz from ACE at 2118:20–2119:20 UT (see Figure 2c) when TH-A moved across the MP. We use $V_\mathrm{sw} = 627$ km/s as the one 64 s cadence plasma measurement in this 1 min interval, which is representative of a solar wind speed for the IMF $Bz < 0$ period after 2117 UT (see Figure 2d). However, from Figure 2g, we conclude that N_sw may be more uncertain after the data gap in plasma measurements than before this gap due to more noticeable differences between a shocked solar wind density ($N_\mathrm{MS} = 4N_\mathrm{sw}$) and the plasma density (N_p) that TH-A observed in the magnetosheath at 2119–2120 UT and 2122–2124 UT. These densities showed a better agreement before the data gap as demonstrated for the earlier 2102–2104 UT excursion into the magnetosphere by TH-A during a northward IMF $Bz > 0$ interval. The three proposed MP model locations in Figure 1, therefore, vary by using three different N_sw values. The upstream density observed by ACE at 2118:20–2119:20 UT ($N_\mathrm{sw} = 1.2$ cm^{-3}) results in the MP surface shown in red for $Dp = 0.76$ nPa (cf. Figure 2e) with a subsolar standoff distance $R_0 = 11.50$ R_E at $Z_\mathrm{GSM} = 0$. However, considering a rather steady IMF $Bz < 0$ and $R_0 > 11$ R_E (see $R_0 = X_\mathrm{MP}$ in Figure 2f) after 2117 UT, it is likely that $Dp < 1$ nPa is too low to explain how THEMIS could exit the MP at 2119 UT. The MP surface shown in blue with $R_0 = 9.65$ R_E used a mean $N_\mathrm{p} = 14.7$ cm^{-3} that TH-A measured in the adjacent magnetosheath at 2119:00–2119:20 UT to suggest an upstream $N_\mathrm{sw} = N_\mathrm{p}/4$ or $N_\mathrm{sw} = 3.7$ cm^{-3} and $Dp = 2.41$ nPa after 2119 UT. A final model MP surface is shown in black with $R_0 = 10.53$ R_E that puts TH-A just sunward of the MP at 2119:00 UT for a proposed $Dp = 1.35$ nPa ($N_\mathrm{sw} = 2.06$ cm^{-3}) and IMF $Bz = -2.7$ nT. The increasingly southward IMF $Bz < 0$ after ~2117–2118 UT likely initiated an active period of enhanced magnetic reconnection at the dayside MP, which, together with the fast >600 km/s solar wind speed (Figure 2d) and a probable $1.0 < Dp < 2.4$ nPa solar wind dynamic pressure (see Figures 1 and 2), eroded and pushed the MP earthward across THEMIS at 2119:00 UT.

Figure 3 provides an enlarged view of magnetic field and plasma observations by the TH-A satellite at 2117–2125 UT when it encountered the two consecutive MP current sheets as highlighted between two pairs of vertical dotted lines. The two MP layers are separated by a short ~1 min period from 2119:00 to 2120:10 UT when TH-A sampled a high-density and low-temperature magnetosheath, which is clear from a lack of high-
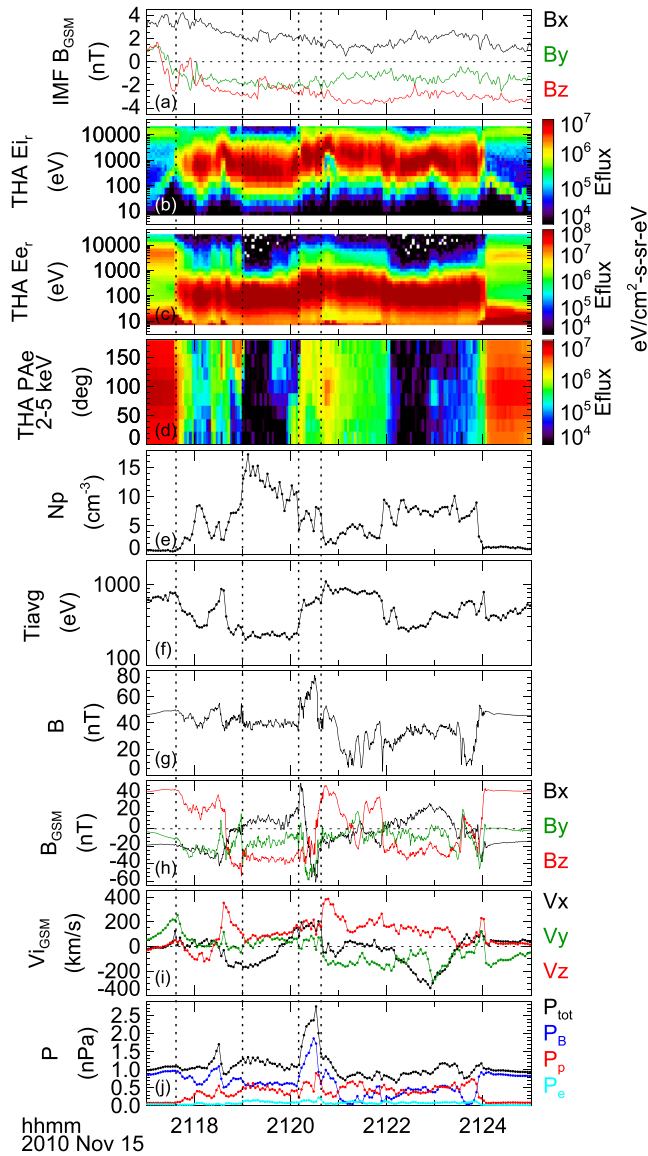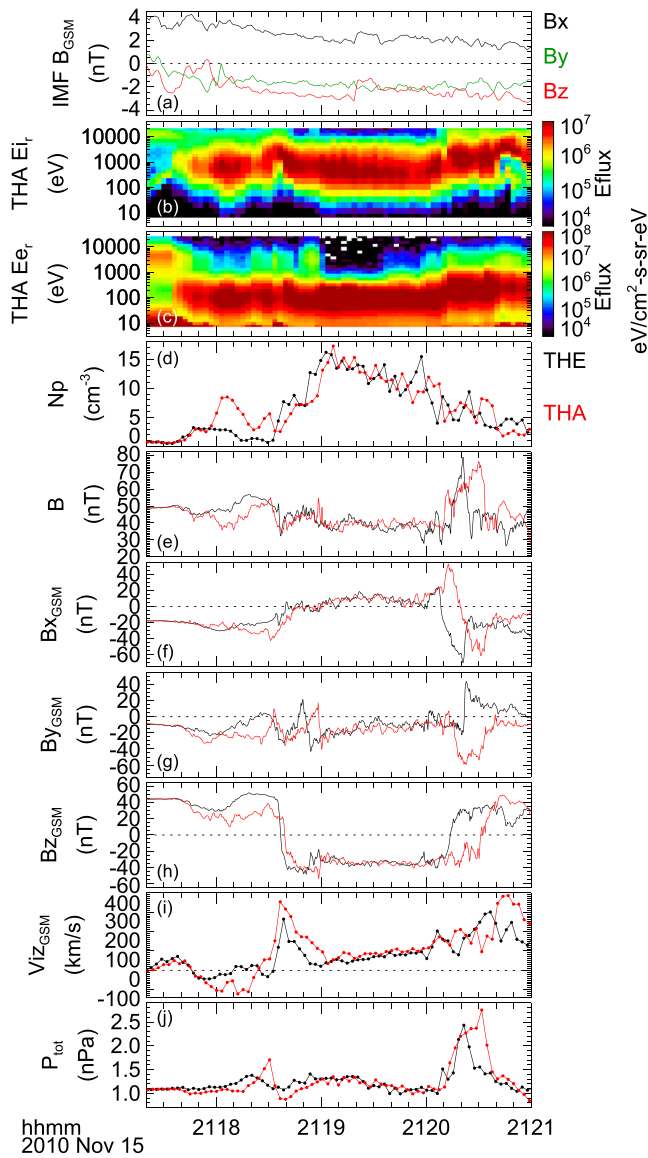
Figure 3. (a) Time-shifted ACE IMF observations at 2117–2125 UT on 15 November 2010. The bottom panels display TH-A observations for the same time period: (b) omnidirectional ion energy-time spectra, (c) omnidirectional electron energy-time spectra, (d) pitch angle distribution of 2–5 keV electron energy fluxes, (e) ion plasma density, (f) average ion temperature, (g) magnetic field strength, (h) magnetic field (GSM), (i) ion velocity (GSM), and (j) color-coded pressure observations. The focus of this study is the two highlighted magnetopause encounters between a pair of vertical dotted lines at 2117:37–2119:00 UT and 2120:10–2120:38 UT. TH-A is located at $[x, y, z]_{GSM} = [10.1, -0.8, 3.8]\ R_E$ at this time.

energy ions and a general absence of electrons of magnetospheric origin in the omnidirectional energy-time spectrograms (see Figures 3b–3f). Figure 3d shows a pitch angle distribution of 2–5 keV magnetospheric electron energy fluxes. A weak flux of field-aligned electrons is observed in the magnetosheath adjacent to the second MP crossing, indicating an escape of high-energy magnetospheric electrons across the MP along an open magnetic field. TH-A eventually entered into the magnetosheath a second time at ~2122:00–2123:30 UT. Both intervals of magnetosheath observations were characterized by $Bx > 0$, $By < 0$, and $Bz < 0$ with $|Bz| > |By|$ (see Figure 3h), which is in general agreement with the time-shifted ACE observations of the IMF at this time as shown in Figure 3a. We note that Hoilijoki et al. (2019) propose that these IMF conditions could result in relatively smaller, and more frequent, FTE flux ropes at the northern dayside MP location of the THEMIS satellites.

Figure 3g shows that the magnetic field strength B reached a stable $45 < B < 50$ nT level in the outer magnetosphere before 2117:30 UT and then again in the magnetosphere region after 2124:00 UT. The magnetosheath interval between the two highlighted MP encounters was characterized by a slightly weaker $36 < B < 43$ nT. However, the second MP encounter at 2120:10–2120:38 UT is clearly different in this aspect with an associated, much stronger, peak magnetic field strength of $B = 76.5$ nT. This field is nearly twice as large as that measured in the magnetosheath and clearly stronger than in the magnetosphere during this 8 min interval of TH-A observations. Figure 3h shows that the enhanced magnetic field is mostly directed in a negative GSM By direction with additional contributions from the GSM Bx component. The Bx component of the magnetic field corresponds roughly to a direction normal to the MP surface just northward of the subsolar point. It displayed a strong positive perturbation at the beginning of the period with the increased negative By and then rotated through $Bx = 0$ near the center of the negative By period before turning into a strong negative Bx perturbation at the end of the By enhancement. The bipolar Bx perturbation around a core $\Delta By < 0$ enhancement and the sense of this bipolar Bx perturbation is consistent with the expected signature of a northward moving FTE-type flux rope along the sunward ($Bz < 0$) side of the MP boundary. Figure 3j shows that the total pressure $P_{tot} = P_B + P_p + P_e$ associated with this flux rope-like magnetic field perturbation also increased, as is often the case for an FTE-type flux rope (e.g., Paschmann et al., 1982), from ~1 nPa before the event to more than 2.5 nPa during the event. Here, P_{tot} is the sum of proton P_p and electron P_e plasma pressures and the magnetic field pressure P_B. The ion ESA instrument measured a fast $Viz = 385$ km/s northward flow (Figure 3i) on the $Bz > 0$ earthward side of the flux rope. The flux rope itself was only associated with a weakly enhanced $Viz = 170$ km/s northward flow and intermediate values of both plasma density and ion temperature (Figures 3e and 3f) between that of the adjacent relatively cold and dense magnetosheath, and the relatively hot and tenuous outer magnetosphere.

Figure 4 compares the simultaneous 2117:20–2121:00 UT observations from TH-A and TH-E during the first, outbound MP crossing and the second, inbound MP encounter. Figure 4f demonstrates that TH-E measured a much smaller positive Bx perturbation than TH-A before the core region of the flux rope was encountered at the second MP, while TH-E observed a large negative Bx perturbation on the earthward $Bz > 0$ (see Figure 4h) side of this MP current sheet. Figure 4e shows that the magnetic field strength of the second MP crossing increased to a similar level at TH-E as that observed at TH-A across the flux rope. However, this is due to the strong negative Bx deflection, not a strong $\Delta By < 0$. In fact, the By component (see Figure 4g)

Figure 4. (a) Time-shifted (39.5 min) ACE IMF observations at 1 s cadence in GSM coordinates; (b) TH-A ion energy-time spectrogram; (c) TH-A electron energy-time spectrogram; (d) ion plasma density; (e) magnetic field strength; (f–h) GSM Bx, By, and Bz components; (i) GSM Vz ion velocity component; (j) total pressure $P_{tot} = P_B + P_p + P_e$. Panels (d–j) compare simultaneous TH-A (red color) and TH-E (black) observations. All observations are shown from 2117:20 to 2121:00 UT on 15 November 2010.

displayed very different signatures between this pair of satellites separated by a total distance of only 0.38 R_E. This apparent difference of the magnetic field as displayed in a GSM coordinate system is better analyzed in an LMN boundary normal coordinate system, as we discuss in section 2.2.

The outbound MP crossing, observed by TH-A from 2117:37 to 2119:00 UT (see Figures 4b–4d), ended just 70 s before the MP encounter with an FTE flux rope. This earlier MP crossing is associated with fast southward then northward Viz flows at the northernmost TH-A satellite (see Figure 4i) as compared with the slower northward directed flows measured in the adjacent magnetosheath. The initial 121 km/s southward jet is only present on the $Bz > 0$ earthward side of the MP boundary layer, while the 353 km/s northward jet straddles the $Bz = 0$ transition of the MP current sheet. The southernmost TH-E satellite, in contrast, only sampled a northward jet across the Bz rotation at the first MP current sheet. The total magnetic field strength did not increase substantially across the first MP boundary, although a local field compression coincident with a plasma density increase observed by TH-A at 2118:30 UT (see Figure 4d) contributed to an observed ~70% increase of the total pressure (see Figure 4j). Rather, TH-A and TH-E both recorded a local B depression in the $Bz = 0$ region of the MP current sheet as compared with the slight B enhancements observed by both satellites immediately earthward and sunward of the Bz reversal. These B enhancements are primarily associated with a strengthening of the local Bz component of the magnetic field on either side of the MP boundary. There are no similar $|Bz|$ increases in the magnetosheath proper after 2119:00 UT, and they are absent from the mostly steady IMF observations recorded by ACE and shown in Figure 4a. Moreover, Figure 3d displays an enhanced energy flux of magnetospheric electrons streaming in the antiparallel (northward) direction along this enhanced $Bz < 0$ magnetic field, while field-aligned magnetospheric electrons are absent, indicating that this magnetic field is open and connected to Earth. The times of enhanced $|Bz|$ on either side of where $Bz = 0$ are observed to coincide with corresponding $|By|$ depressions of the mostly negative By component at TH-A and TH-E, while $|By|$ recovers across the central $Bz = 0$ region, such that the By signatures across the MP are reminiscent of those first reported as tripolar out-of-plane perturbations in Polar satellite observations at the subsolar MP (Eriksson et al., 2016).

TH-D remained in the low-density (N_p ~ 1 cm^{-3}) outer magnetosphere until 2118:40 UT (not shown) when the satellite rapidly traversed the MP current sheet from $Bz > 0$ into the adjacent magnetosheath $Bz < 0$ boundary layer, which is characterized by a presence of weaker energy fluxes of high-energy magnetospheric electrons. TH-D observed the same strengthening of a negative Bz coincident with a positive By rotation across a northward Viz jet within this magnetosheath boundary layer as did TH-A and TH-E. However, TH-D neither sampled the southward Viz jet that TH-A encountered earthward of the first MP, nor the initial sequence of a negative-then-positive By variation within a low-latitude boundary layer (LLBL) that TH-A and TH-E sampled during a prolonged 1 min interval from ~2117:40 UT to 2118:40 UT on the earthward $Bz > 0$ side of this first MP. Considering the relative proximity of TH-D to the other satellites, with a $\Delta Y_{GSM} = 0.575$ R_E separation between TH-D and TH-A, it appears that the tripolar By magnetic field structures within a higher-density LLBL mixing region are spatially limited. We focus the remainder of this section of observations on contrasting the differences and similarities that TH-A and TH-E measured in

magnetic fields and ion particle signatures across the two MP encounters in a local boundary normal LMN coordinate system.

2.2. Observations in Boundary Normal Coordinates

We transform magnetic fields and ion velocity moments from the GSM coordinate system into a fixed LMN boundary normal system to allow for detailed interspacecraft comparisons of the magnetic field structures and ion velocity changes relative to the local MP current sheet. We apply a minimum variance (MVAB) analysis (Sonnerup & Scheible, 1998) of the 0.25 s cadence magnetic field that TH-E observed between 2117:29.8 UT and 2119:04.0 UT with eigenvalues $[\lambda_1, \lambda_2, \lambda_3] = [21.1, 108.2, 1370.0]$ $(nT)^2$. This interval incorporates the first complete MP crossing with a 138° magnetic field rotation angle from the geomagnetic field $\mathbf{B}_{GSM} = [-17.6, -10.0, 44.6]$ nT to the magnetosheath field $\mathbf{B}_{GSM} = [8.1, -17.9, -30.1]$ nT. The resulting-boundary normal direction $\mathbf{N}_{GSM} = [0.932488, -0.245197, 0.265224]$ and the direction of maximum variance $\mathbf{L}_{GSM} = [-0.252990, 0.080716, 0.964096]$ define a dawnward, out-of-plane direction ($\mathbf{M} = \mathbf{N} \times \mathbf{L}$) of a right-handed, orthogonal LMN system with $\mathbf{M}_{GSM} = [-0.257802, -0.966107, 0.013235]$.

Figure 5 displays a side-by-side comparison of TH-A and TH-E observations in this fixed LMN boundary coordinate system from 2117:20 UT to 2121:00 UT. The two satellites observed a characteristic B_M variation (see Figures 5g and 5s) across the first MP current sheet with enhanced total pressure at TH-A (see Figure 5l) but without an obvious FTE flux rope in the absence of a bipolar B_N variation of the normal magnetic field. The B_M variation displays an initial B_M increase, which is followed by a tripolar ΔB_M signature. The tripolar variation consists of two substantial B_M decreases separated by a localized B_M recovery at the time of the $B_L = 0$ transition (see Figures 5f and 5r). A Walén prediction, $V_L = V_{L0} \pm [(1 - \alpha_0)\rho_0/\mu_0]^{1/2}(B_L/\rho - B_{L0}/\rho_0)$, is displayed as the red and blue traces in Figure 5i for the TH-A interval 2118:33.2–2118:52.4 UT, and in Figure 5u for the TH-E interval 2118:34.0–2118:50.4 UT across the northward flow enhancement of the first MP current sheet. The red traces correspond to $V_L = V_{L0} - \Delta V_L$ from the magnetosphere side of the current sheet and the blue traces correspond to $V_L = V_{L0} + \Delta V_L$ from the magnetosheath side of the current sheet into the jet. This pressure anisotropy-weighted expression (Paschmann et al., 1986) is based on the high-cadence B_L magnetic field and spin cadence plasma parameters ($\rho = Nm_p$ and α) interpolated to this B_L magnetic field. Subscripts "0" refer to values in the two external regions. The ion pressure anisotropy $\alpha \equiv (P_{para} - P_{perp})\mu_0/B^2$ is obtained from the ion temperatures parallel and perpendicular to the magnetic field (not shown). The good agreement with the measured Vi_L for both satellites confirms that this jet is consistent with a northward reconnection exhaust from a southern X-line.

The subsequent MP encounter that we associate with an FTE-type flux rope displays a very symmetric positive-then-negative bipolar variation of the normal B_N component of the magnetic field (see Figure 5h) at TH-A consistent with a northward moving helical flux rope (e.g., Cowley, 1982). In contrast, while TH-E observed very similar magnetic fields in all three LMN components as TH-A did in the preceding magnetosheath interval, it observed a very different magnetic field along this inbound trajectory near the FTE flux rope as compared with TH-A. First, the B_N component (see Figure 5t) displayed a very asymmetric, positive-then-negative bipolar variation that remained negative ($B_N < 0$) earthward of the flux rope. Second, the two satellites observed very different B_M signatures. TH-A observed a highly asymmetric bipolar B_M across the FTE flux rope with a weak and narrow duskward $\Delta B_M < 0$ on the sunward side of what we interpret as a dawnward $\Delta B_M > 0$ core region of the flux rope. TH-A encountered this FTE core field mostly on the $B_L < 0$ side of the MP current sheet (see Figures 5f and 5g). However, TH-E once again observed a very clear, tripolar ΔB_M signature across this second MP encounter near the FTE flux rope as it had recorded across the first MP current sheet without an obvious FTE flux rope. It starts with a similarly weak and narrow $\Delta B_M < 0$ on the magnetosheath side, just as TH-A observed, followed by a modest $\Delta B_M > 0$ core field and, finally, TH-E observed a significant duskward $\Delta B_M < 0$ deflection on the earthward $B_L > 0$ side of the flux rope. The northernmost TH-A satellite did not record this large duskward $\Delta B_M < 0$ depression in the LLBL. Finally, neither THEMIS satellite recorded a southward Vi_L jet (see Figures 5i and 5u) from the ion moments of the distribution at this second MP current sheet to support a northern X-line. Rather, the ion moments indicated a positive and variable Vi_L across the flux rope at both satellites, while a prominent northward $Vi_L > 0$ jet from a southern X-line was clearly present on the earthward ($B_L > 0$) side of the flux rope at both locations.
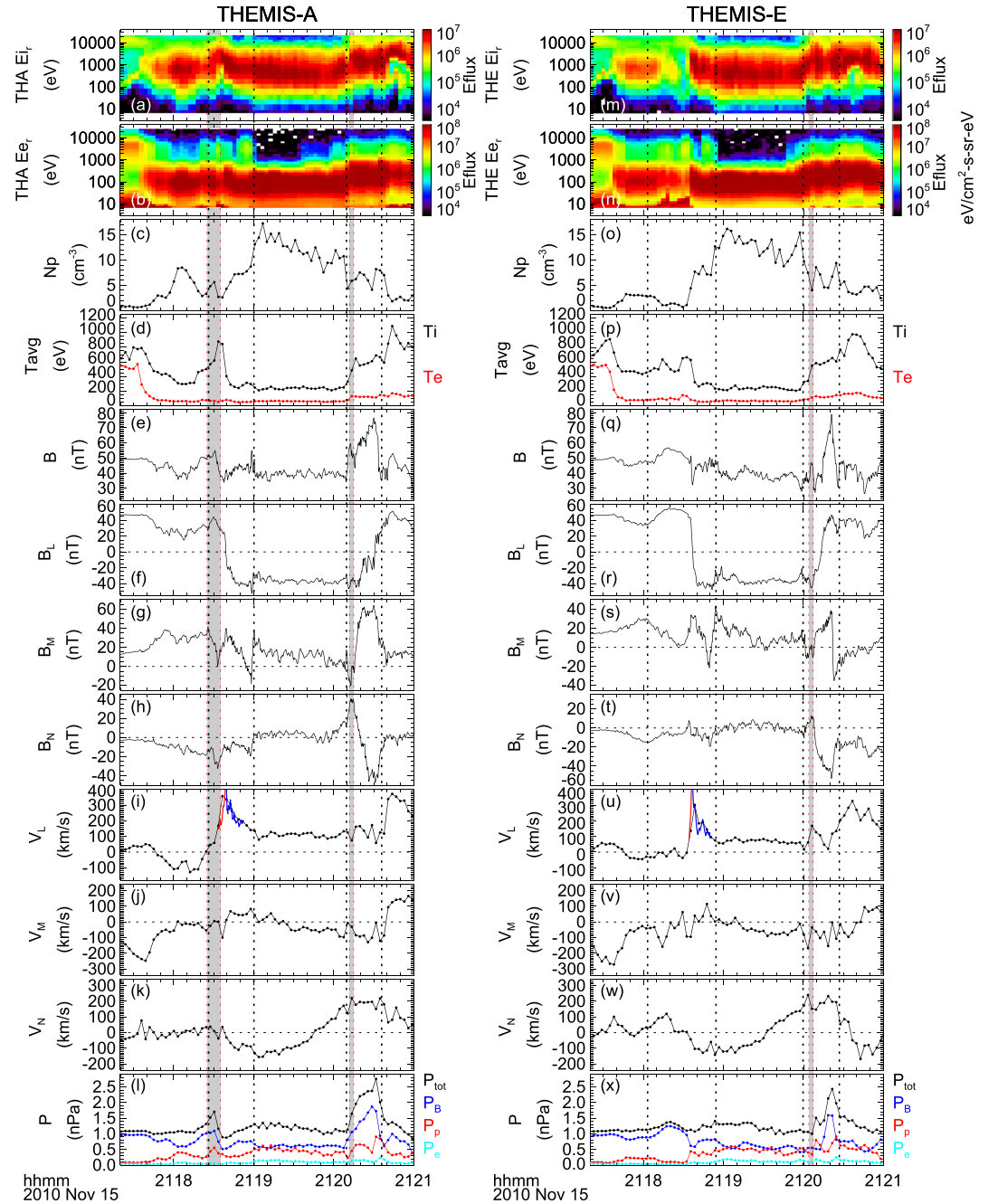
Figure 5. TH-A (a–l) and TH-E (m–x) observations are compared side by side at 211720–212100 UT: (a, m) Omnidirectional ion energy-time spectrogram; (b, n) omnidirectional electron energy-time spectrogram; (c, o) ion plasma density; (d, p) average ion (black) and electron (red) temperatures; (e, q) magnetic field strength; (f, r) L component of the magnetic field; (g, s) M component of the magnetic field; (h, t) N component of the magnetic field; (i, u) L component of ion velocity; (j, v) M component of ion velocity; (k, w) N component of ion velocity; (l, x) total pressure (black) and its contributions from the magnetic field pressure (blue), ion plasma pressure (red) and electron plasma pressure (cyan). The red and blue traces in panels (i) and (u) display the pressure anisotropy-weighted Walén prediction $V_L = V_{L0} \pm \Delta V_L$ where $\Delta V_L = [(1 - \alpha_0)\rho_0/\mu_0]^{1/2}(B_L/\rho - B_{L0}/\rho_0)$. The two pairs of black, vertical dotted lines mark a tripolar ΔB_M signature across the first outbound MP crossing and a mature FTE flux rope across the second inbound MP crossing. Shaded vertical regions mark the time intervals of a few ion velocity distribution functions as shown in Figures 6 and 7. TH-A is located at $[x, y, z]_{GSM} = [10.1, -0.8, 3.8]\ R_E$, and TH-E is located at $[x, y, z]_{GSM} = [10.3, -0.6, 3.5]\ R_E$ at this time.
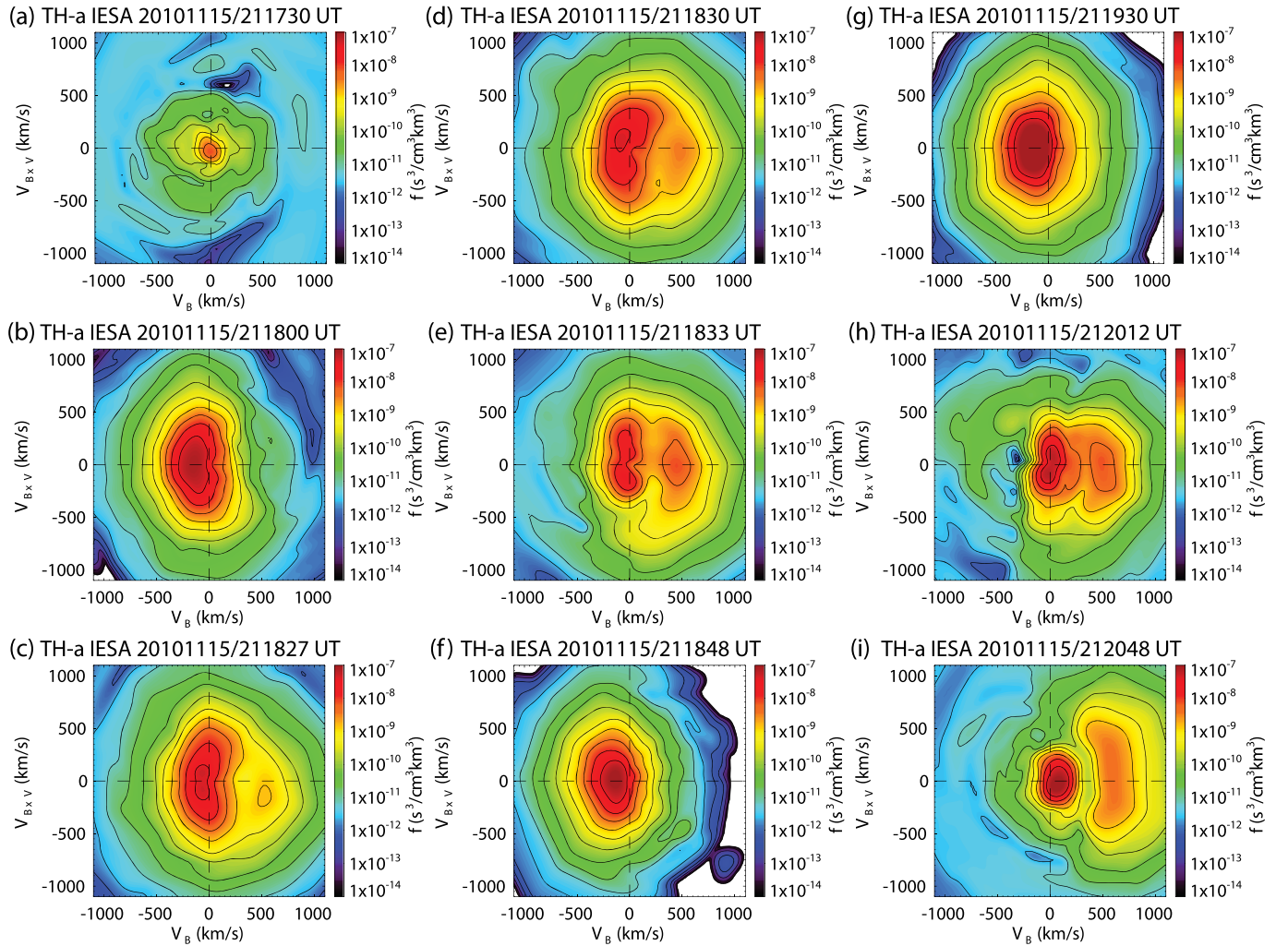
Figure 6. TH-A (3 s) reduced ion velocity distribution functions (VDF) in a plane defined by the field-parallel direction (V_B) and the field-perpendicular direction along the convection electric field ($V_{B\times V}$): (a) low-density magnetosphere at 2117:31–2117:34 UT; (b) southward jet at 2117:58–2118:01 UT when $B_L > 0$; (c–e) three consecutive ion VDFs during the jet transition when $B_L > 0$ and first $\Delta B_M < 0$ dip at 2118:25–2118:28 UT, 2118:28–2118:32 UT, and 2118:32–2118:35 UT; (f) northward jet at 2118:47–2118:50 UT when $B_L < 0$; (g) ion VDF in the magnetosheath at 2119:29–2119:32 UT; (h) flux rope ion VDF at 2120:12–2120:15 UT when $B_L < 0$, $B_M < 0$, and $B_N > 0$; (i) northward jet at 2120:48–2120:51 UT on earthward side of flux rope when $B_L > 0$.

2.3. Ion VDF Observations

Figure 6 provides a set of ion VDFs that TH-A recorded around the first MP current sheet (Figures 6a–6f), in the magnetosheath proper at 2119:30 UT (Figure 6g) and across the second FTE-related MP (Figures 6h and 6i). Each ion VDF is obtained during a complete 3 s spin period of the satellite. The first ion VDF at 2117:30 UT (Figure 6a) is representative of the tenuous, outer magnetosphere population. The ion distribution sampled in the LLBL at 2118:00 UT (Figure 6b) displays a roughly D-shaped antiparallel beam of magnetosheath ions (Cowley, 1982) as compared with the more isotropic magnetosheath population (see Figure 6g), the core of which is drifting northward or opposite the southward $B_L < 0$ magnetic field. In contrast, the LLBL magnetic field is predominantly northward $B_L > 0$ when TH-A recorded the ion distribution of Figure 6b during the first $\Delta B_M > 0$ perturbation. That is, the antiparallel-propagating magnetosheath ions of this southward Vi_L exhaust may have entered the LLBL near an X-line northward of TH-A. Figure 6f displays a similar, mostly antiparallel ion beam distribution that TH-A sampled around 2118:48 UT. However, these ions drift northward, since this ion VDF is obtained clearly on the $B_L < 0$ side of the MP current sheet (see Figure 5f). The distribution is also more anisotropic, as compared with the isotropic ion VDF in the magnetosheath proper, which is consistent with a northward ion exhaust from an X-line to the south of TH-A.
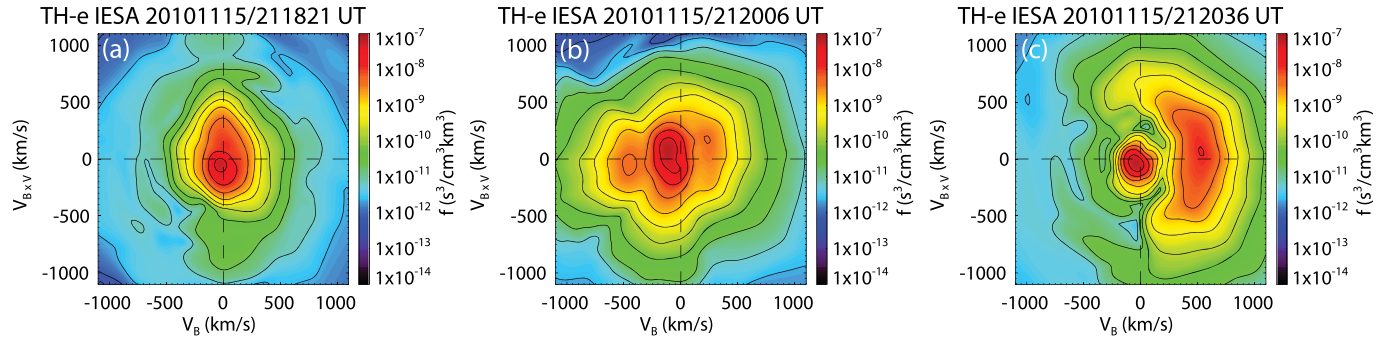
Figure 7. TH-E (3 s) reduced ion velocity distribution functions (VDF) in a plane defined by the field-parallel direction (V_B) and the field-perpendicular direction along the convection electric field (V_{BxV}): (a) LLBL mixing region at time of first $\Delta B_M < 0$ dip 2118:21–2118:24 UT; (b) flux rope ion VDF at 2120:04–2120:07 UT when $B_L < 0$, $B_M < 0$, and $B_N > 0$; (c) northward jet at 2120:35–2120:38 UT on earthward side of flux rope when $B_L > 0$.

The three consecutive ion VDFs shown in Figures 6c–6e sampled the region between the two oppositely directed ion exhausts at 2118:25–2118:35 UT. Figure 5 (left) marks this interval using a shaded vertical bar. The three ion VDFs display two separate, counterstreaming ion beams along the $B_L > 0$ magnetic field that TH-A measured during the first substantial $\Delta B_M < 0$ perturbation of a tripolar B_M magnetic field. The sequence illustrates an apparent transition of the two counterstreaming ion beams in velocity space, which could be spatial in nature as we discuss in section 4. The phase space density of the initially dominant antiparallel (southward) ion beam at 2118:27 UT from a northern X-line decreases as the phase space density of the parallel-streaming ions grows into a D-shaped northward ion beam from a southern X-line that dominates over the antiparallel ion beam at 2118:33 UT, which is also reflected by a northward Vi_L component of the ion velocity moment at this time as shown in Figure 5i. Two active X-lines at the dayside MP current sheet can explain the counterstreaming magnetosheath ion beams in this $B_L > 0$ region of the LLBL.

Figure 6h presents the ion VDF that TH-A measured at 2120:12 UT on the $B_L < 0$ magnetosheath side of the second MP crossing. The 3 s duration of this ion VDF interval, which is marked as the second shaded vertical bar in Figure 5 (left), occurred within the first duskward $\Delta B_M < 0$ perturbation coincident with the peak $B_N > 0$ region of the FTE and immediately before the $\Delta B_M > 0$ core region of the FTE flux rope. The distribution displays one fast, roughly D-shaped, field-aligned ion beam, which is streaming southward along the $B_L < 0$ magnetic field. There is also one slow, antiparallel ion population with high ion phase space density that could be associated with a magnetosheath source, such that the integrated VDF results in a northward $Vi_L = 74$ km/s flow (cf. Figure 5i) in agreement with the dominant magnetosheath flow direction. However, the D-shaped southward ion beam strongly suggests the presence of an X-line poleward of TH-A before the satellite entered the core region of this FTE flux rope. There is also strong evidence for the presence of an active X-line equatorward of TH-A from the fast northward exhaust and the field-aligned, D-shaped ion VDF (see Figure 6i) that TH-A measured along the $B_L > 0$ magnetic field on the LLBL side of the flux rope at 2120:48 UT.

TH-E did not measure any counterstreaming ion beams in the first $\Delta B_M < 0$ region from 2118:15 to 2118:27 UT of the first MP crossing, as TH-A did in three consecutive measurements between the two converging exhausts. Rather, it measured a magnetospheric-like ion population (see Figure 7a) reminiscent of the magnetospheric ion VDF shown in Figure 6a, in general agreement with a lower plasma density of this LLBL mixing region (cf. Figures 5m–5o) than TH-A observed (cf. Figures 5a–5c). Further, TH-E did not observe a clearly D-shaped, southward ion beam along the $B_L < 0$ magnetic field on the magnetosheath side of the flux rope as TH-A did at 2120:12 UT. Instead, TH-E recorded an intriguing ion VDF (see Figure 7b) within the first duskward $\Delta B_M < 0$ depression of a tripolar B_M field that consisted of two separate, antiparallel-propagating (northward) ion populations at 2120:06 UT and a third, weakly southward drifting (parallel) ion population. Figure 5 (right) marks this 3 s VDF interval with a shaded vertical bar. We interpret this ion VDF as consisting of two counterstreaming ion beams of low phase space density, surrounding a dominant core population of slowly northward
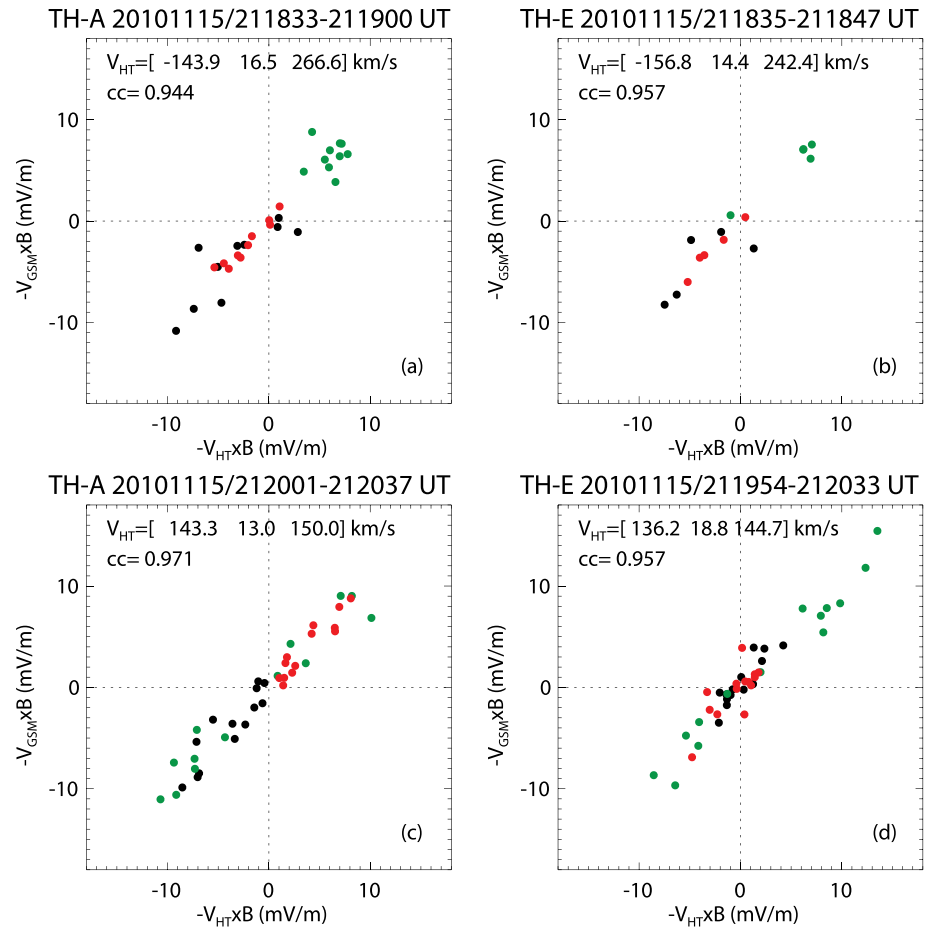
Figure 8. deHoffmann-Teller (HT) analyses resulting in moving frames of reference for TH-A (left) and TH-E (right) at the times of the first (top: a, b) and the second (bottom: c, d) magnetopause encounters. GSM convection electric fields are shown for each time interval with color representing X_{GSM} (black), Y_{GSM} (green), and Z_{GSM} (red). Correlation coefficients and HT frame velocities $\mathbf{V}_{\mathrm{HT}}$ in GSM coordinates are stated in each panel.

drifting magnetosheath ions of high phase space density. TH-E also measured a fast field-aligned and D-shaped ion beam from a southern X-line at 2120:36 UT on the earthward side ($B_{\mathrm{L}} > 0$) of the MP current sheet as shown in Figure 7c. It is very similar to the D-shaped ion beams observed by TH-A at 2120:48 UT (see Figure 6i) on this earthward LLBL side of the MP.

3. Spatial Dimension Analyses of THEMIS Observations

We summarize the THEMIS observations across the two back-to-back MP encounters on 15 November 2010 with an illustration of the magnetic field (**B**) and ion velocity (Vi_{L}) along the two satellite trajectories through two plausible magnetic field structures. We first employ a deHoffmann-Teller (HT) frame analysis (Khrabrov & Sonnerup, 1998) to obtain a structure velocity $\mathbf{V}_{\mathrm{HT}}$ for each satellite across the two consecutive MP encounters. Figure 8 depicts the resulting convective electric field observations in the obtained HT frames of reference for each satellite. Each panel provides the HT analysis time interval, the HT structure velocity in GSM coordinates and the correlation coefficients between the measured ion $-\mathbf{V}_{\mathrm{GSM}} \times \mathbf{B}_{\mathrm{GSM}}$ and the resulting $-\mathbf{V}_{\mathrm{HT}} \times \mathbf{B}_{\mathrm{GSM}}$. We rotate each of the four $\mathbf{V}_{\mathrm{HT}}$ from GSM into the LMN coordinate system that we used earlier for **B** and $\mathbf{V}_{\mathrm{i}}$. Both satellites record a similar northward structure velocity across the first MP current sheet, $[V_{\mathrm{HTL}}, V_{\mathrm{HTM}}, V_{\mathrm{HTN}}] = [294.77, 24.69, -67.51]$ km/s at TH-A and $[V_{\mathrm{HTL}}, V_{\mathrm{HTM}}, V_{\mathrm{HTN}}] = [274.54, 29.69, -85.44]$ km/s at TH-E. The earthward directed $V_{\mathrm{HTN}} < 0$ of the MP boundary motion is consistent with an outbound MP crossing of the satellites. The HT structure velocities of the second MP encounter with an FTE flux rope also compare very well at the two satellites, $[V_{\mathrm{HTL}}, V_{\mathrm{HTM}},$

$V_{\mathrm{HTN}}] = [109.38, -47.51, 170.17]$ km/s at TH-A and $[V_{\mathrm{HTL}}, V_{\mathrm{HTM}}, V_{\mathrm{HTN}}] = [106.60, -51.38, 160.74]$ km/s at TH-E. The positive $V_{\mathrm{HTN}} > 0$ reflects a sunward MP motion consistent with an inbound MP crossing of the satellites. It is also clear from the in-plane magnitudes $V_{\mathrm{NL}} = (V_{\mathrm{N}}^2 + V_{\mathrm{L}}^2)^{1/2}$ of these HT frame velocities that the second MP-associated flux rope drifted about 100 km/s slower across the satellites than the magnetic field structures of the first MP.

The HT frame velocities of Figure 8 can be used to define the NL plane trajectory of the two satellites through the MP boundary from $\tan(\alpha) = |V_{\mathrm{HTN}}/V_{\mathrm{HTL}}|$ such that $\alpha = 90°$ corresponds to a trajectory along the MP normal direction. The similar α direction angles for the first MP crossing (12.9° and 17.3°) and the second MP encounter (57.3° and 56.4°) suggest that we may average the two HT structure velocities for TH-A and TH-E across each separate MP boundary. Figure 9 displays the resulting satellite trajectories of TH-A and TH-E across the two MP current sheets that also include the known NL plane separation of the two satellites. The accumulated spatial distances are transformed into ion inertial lengths $Li = c/\omega_{\mathrm{pi}}$ using a fixed $Li = 99.96$ km for both satellites for a more straightforward interspacecraft comparison. This $Li = 99.96$ km value is obtained by TH-A across the first MP boundary layer for a measured average plasma density $N_{\mathrm{p}} = 5.8$ cm^{-3} at 2118:27–2118:57 UT. We display the two outbound satellite trajectories for the time interval between 2117:38.5 UT and 2119:00.2 UT, with dots marking the start of each trajectory. TH-A trails TH-E almost perfectly through the first MP boundary in this NL plane from a combination of $\mathbf{V}_{\mathrm{HT}}$ and satellite separation. We use a start location of the two subsequent inbound trajectories (dots) that includes a southward displacement of $\Delta L \sim 130\ Li$ from the end locations of the outbound section, which is obtained using the northward magnetosheath speed during the 70 s separation between the two MP encounters. The inbound section is limited to the time interval 2120:00.1–2120:41.4 UT.

Table 1 provides reference values of the LMN magnetic field for TH-A and TH-E in the magnetosphere, prior to the first $\Delta B_{\mathrm{M}} > 0$ enhancement in the LLBL, and in the adjacent magnetosheath for the first MP current sheet. The satellites observed a very similar $B_{\mathrm{M}}/B_{\mathrm{L}} = 0.35$ guide field ratio in the magnetosphere as the Polar satellite observed across a similar tripolar B_{M} structure (Eriksson et al., 2016). The $B_{\mathrm{M}}/B_{\mathrm{L}}$ ratio is only slightly more elevated in the magnetosheath. We define a background guide magnetic field across this first MP crossing, $B_{\mathrm{G}} = 15.9$ nT, as the average of the four B_{M} values measured by TH-A and TH-E on either side of this MP boundary. Table 2 provides LMN reference values of the magnetic field for TH-A and TH-E in the magnetosheath, prior to the first $\Delta B_{\mathrm{M}} < 0$ enhancement, and in the adjacent LLBL for the second MP current sheet. The satellites observed a similar, but somewhat lower, $B_{\mathrm{M}}/B_{\mathrm{L}} = 0.2$ guide field ratio adjacent to the FTE flux rope. We note that the background guide magnetic field, $B_{\mathrm{G}} = 8.6$ nT, obtained as the average of the two B_{M} values measured by TH-A and TH-E in the magnetosheath, is weaker for this inbound MP crossing as compared with $B_{\mathrm{G}} = 15.9$ nT of the outbound MP crossing.

Figure 9a displays the out-of-plane variations $\Delta B_{\mathrm{M}} = B_{\mathrm{M}} - B_{\mathrm{G}}$ along each satellite trajectory in red color for $\Delta B_{\mathrm{M}} > 0$ and in blue color for $\Delta B_{\mathrm{M}} < 0$ with $B_{\mathrm{G}} = 15.9$ nT for the outbound MP crossing and $B_{\mathrm{G}} = 8.6$ nT for the inbound MP encounter. Figures 9b and 9c display the same out-of-plane ΔB_{M} information as in Figure 9a but using a cyan color for $\Delta B_{\mathrm{M}} > 0$ regions. In addition, Figure 9b displays every fourth data point of the in-plane 4 Hz magnetic field vectors, $\mathbf{B}_{\mathrm{NL}} = \mathbf{B}_{\mathrm{N}} + \mathbf{B}_{\mathrm{L}}$, along each satellite trajectory. Figure 9c displays the measured Vi_{L} ion flow component in the satellite frame of reference along each trajectory for a straightforward comparison with the time series observations of Figure 5. The additional vector information ($\mathbf{B}_{\mathrm{NL}}$ and Vi_{L}) along the two satellite trajectories of Figures 9b and 9c are shown as red vectors for TH-A and black vectors for TH-E.

We use the in-plane magnetic fields of Figure 9b and the evidence of two active X-lines for each MP encounter, as discussed earlier, to render the proposed outline of two magnetic island structures. The out-of-plane ΔB_{M} perturbations across the northern magnetic island of the Figure 9 schematic suggest that the initial dawnward $\Delta B_{\mathrm{M}} > 0$ extends deep into the interior of this island. This dawnward $\Delta B_{\mathrm{M}} > 0$ also coincides with a southward Vi_{L} exhaust on the earthward LLBL side of $B_{\mathrm{L}} = 0$ (e.g., Figures 5g and 5i) from a northern X-line, in agreement with the expected earthward shift of exhausts in asymmetric plasma density conditions across the MP (Cassak & Shay, 2007). However, Hall magnetic fields are not expected to be this pronounced on the earthward side for asymmetric MP conditions (e.g., Karimabadi et al., 1999). A question is whether this positive $\Delta B_{\mathrm{M}} > 0$ deep inside the LLBL region may be explained in terms of a superposition of the $B_{\mathrm{G}} > 0$ guide field in the adjacent magnetosheath with a positive Hall field.
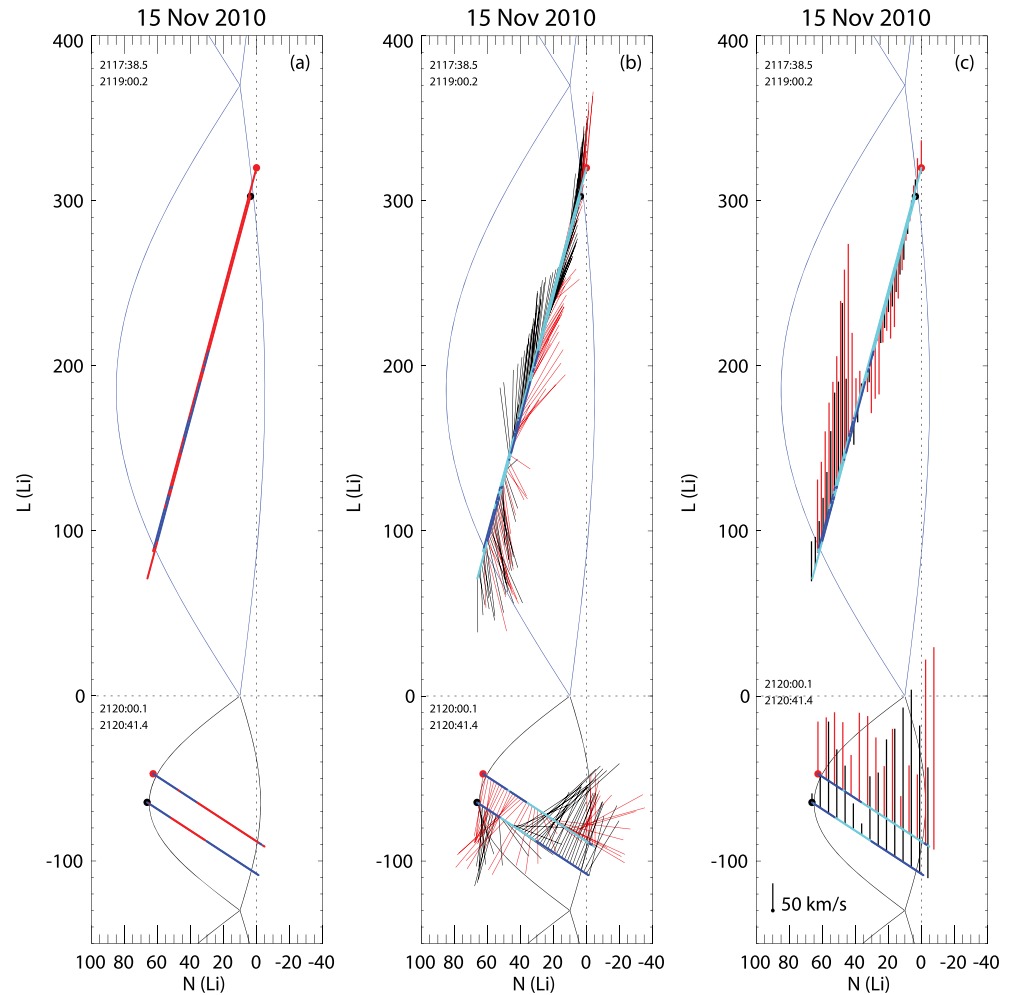
Figure 9. Satellite trajectory representations of TH-A and TH-E magnetic field observations in the NL plane on 15 November 2010 with $\mathbf{M} = \mathbf{N} \times \mathbf{L}$ positive into the plane of the figure. We employ the average of the two HT frame velocities from TH-A and TH-E for each MP crossing and thus obtain the spatial orientations of the satellite trajectories: (a) red color segments correspond to times when $\Delta B_M = B_M - B_G > 0$, and blue color segments correspond to sections of $\Delta B_M < 0$ along each trajectory. The guide field $B_G = 15.9$ nT for the outbound crossing and $B_G = 8.6$ nT for the inbound crossing; (b) low-resolution (1 Hz) NL plane $\mathbf{B}$ along each trajectory; (c) Vi_L along each trajectory. Red color segments along each trajectory in Panel (a) are shown in cyan color in Panels (b) and (c) for clarity. In-plane $\mathbf{B}$ and Vi_L are shown in black for TH-E and red color for TH-A. Geometric shapes and locations of proposed magnetic islands are rendered on the basis of visual inspections of the measured NL plane $\mathbf{B}$. Spatial distances are transformed into ion inertial lengths using an average density $N_p = 5.8$ cm^{-3} or $Li = 99.96$ km as measured by TH-A at 2118:27–2118:57 UT in the outer part of the first MP boundary layer. TH-E is separated by $[\Delta X, \Delta Y, \Delta Z] = [11.8, 13.6, -16.5]$ Li (GSM) from TH-A, or $[\Delta L, \Delta M, \Delta N] = [-17.8, -16.4, 3.3]$ Li. Red (TH-A) and black (TH-E) dots denote trajectory start locations.

The subsequent tripolar ΔB_M perturbations that surround the $B_L = 0$ region of the proposed northern magnetic island and out toward the magnetosheath is of the same sense as the tripolar ΔB_M signature that TH-E recorded along its inbound path near a mature FTE flux rope. The presence of a fast northward directed ion exhaust toward the magnetosheath side of this earlier tripolar ΔB_M observation suggests that it is associated with magnetic reconnection.

The two proposed magnetic islands of Figure 9 between two X-lines likely represent two spatially separate magnetic field structures due to the faster northward HT drift of the first structure as compared with the slower northward HT drift of the FTE flux rope. We associate the southern magnetic island of Figure 9 with a mature FTE flux rope. The northern magnetic island may correspond to an early (nascent) stage of a so-called crater FTE flux rope on the basis of a total pressure enhancement observed by TH-A and local depressions of

Table 1

LMN Reference Magnetic Fields Across the First MP Current Sheet for TH-A and TH-E

Satellite	Time (UT)	B_L (nT)	B_M (nT)	B_N (nT)	B_M/B_L
TH-A MSP	2117:38.5	46.8	16.0	−2.8	0.34
TH-E MSP	2117:39.5	47.1	16.7	−3.2	0.35
TH-A MSH	2119:05.2	−35.6	14.9	3.1	0.42
TH-E MSH	2119:00.4	−34.6	16.1	1.6	0.47

Note. Averages of 0.25 s cadence magnetic fields are 5 s in duration prior to the listed outer magnetosphere (MSP) times and after the listed magnetosheath (MSH) times.

the total magnetic field observed by TH-A and TH-E across $B_L = 0$ in a region which is otherwise associated with modest increases of the magnetic field strength on both sides of the first MP current sheet (e.g., Chen et al., 2017; Zhang et al., 2010).

Table 3 summarizes the duration and corresponding spatial dimensions of each $\Delta B_M = B_M - B_G$ segment of the tripolar perturbation across the first MP crossing relative to $B_G = 15.9$ nT. The LMN dimensions are given in terms of a local ion inertial length at TH-A ($Li = 99.96$ km) and we employed the individual, northward directed $\mathbf{V}_{HT}$ structure velocities as stated earlier in LMN coordinates for each satellite (cf. Table 3 caption). The B_M column of Table 3 lists the maximum or minimum B_M value within each segment unless noted otherwise. It is clear that TH-A and TH-E, while separated by 1,640 km along the M axis, or 16.4 Li, observed similar ΔB_M values of substantial magnitude relative to $B_G = 15.9$ nT. The two satellites observed a similar ~6–8 Li normal width of the magnetosheath side $\Delta B_{M2} < 0$. It is also interesting that the northernmost, trailing TH-A satellite observed a more positive core field enhancement $\Delta B_{Mc} > 0$ across $B_L = 0$ than TH-E with a similar ~8–10 Li normal width of this positive ΔB_{Mc} deflection. The normal width of the initial $\Delta B_{M1} < 0$, while being very similar in magnitude at the two satellites, is 19 Li at the leading TH-E satellite, and just over 2 Li wide at the trailing TH-A satellite.

Table 4 displays the corresponding durations and LMN dimensions of the bipolar $\Delta B_M = B_M - B_G$ segments recorded by TH-A, and the tripolar $\Delta B_M = B_M - B_G$ segments measured by TH-E, relative to a magnetosheath $B_G = 8.6$ nT across the FTE flux rope. The local, but slower, $\mathbf{V}_{HT}$ structure velocities are used across this second MP encounter, and we employed the same $Li = 92.09$ km at both satellites for the average $N_p = 6.4$ cm^{-3} boundary plasma density that TH-A measured at 2120:10–2120:34 UT. The normal width of the magnetosheath side $\Delta B_{M2} < 0$ regions relative to $B_G = 8.6$ nT is 11–13 Li, or nearly twice as wide as compared with the 6–8 Li normal widths of the magnetosheath side $\Delta B_{M2} < 0$ regions relative to $B_G = 15.9$ nT recorded at both satellites for the earlier outbound pass. The $\Delta B_{Mc} = 55$ nT core field enhancement of the FTE flux rope relative to $B_G = 8.6$ nT is more than twice as strong in magnitude as compared with ΔB_{Mc} across the $B_L = 0$ transition of the first MP crossing about 100 s earlier, when TH-E measured $\Delta B_{Mc} = 18$ nT and TH-A measured $\Delta B_{Mc} = 24$ nT relative to $B_G = 15.9$ nT. Moreover, the core field of the FTE flux rope covers a normal width of 43 Li, which is nearly twice the 23 Li width of the positive $\Delta B_{Mc} > 0$ field of the tripolar feature that TH-E measured across this flux rope.

4. PIC Numerical Simulation

In order to address the origin of the observed out-of-plane magnetic fields as summarized in Figure 9, we carry out 2.5-dimensional electromagnetic PIC simulations using the *P3D* code (Zeiler et al., 2002). The *P3D* code evolves the relativistic Vlasov-Maxwell equations in time on a Cartesian grid. The electromagnetic fields are stepped forward in time using a second-order trapezoidal leapfrog scheme, while the particles are stepped forward using a relativistic Boris stepper (Birdsall & Langdon, 2004). The divergence constraints in Maxwell's equations are enforced using a divergence cleaning scheme every 10 particle time steps using the multigrid technique (Trottenberg et al., 2000).

4.1. PIC Simulation Setup

Table 2

LMN Reference Magnetic Fields Across the FTE Flux Rope of the Second MP Current Sheet for TH-A and TH-E

Satellite	Time (UT)	B_L (nT)	B_M (nT)	B_N (nT)	B_M/B_L
TH-A MSH	2119:58.1	−38.1	8.9	−1.2	0.23
TH-E MSH	2119:53.3	−38.4	8.2	−1.2	0.21
TH-A LLBL	2120:41.4	49.3	12.4	0.6	0.25
TH-E LLBL	2120:30.4	39.5	−7.4	−16.1	0.19

Note. Averages of 0.25 s cadence magnetic fields are 5 s in duration prior to the listed magnetosheath (MSH) times and 5 s after the listed low-latitude boundary layer (LLBL) times.

Times, lengths, velocities, and temperatures are normalized in the code, respectively, to the reciprocal of the ion cyclotron frequency $\Omega_{ci0}^{-1} = m_i/eB_0$, the ion inertial length $d_{i0} = c_{A0}/\Omega_{ci0}$, the ion Alfvén speed $c_{A0} = B_0/\sqrt{(\mu_0 n_0 m_i)}$, and $T_0 = m_i c_{A0}^2$, where B_0 and n_0 are a reference magnetic field strength and particle number density. The elementary charge, ion mass, and magnetic permeability of free space are denoted e, m_i, and μ_0. Here, $B_0 = 33.9$ nT and $n_0 = 25$ cm^{-3}, with the corresponding $d_{i0} = 45.54$ km, $c_{A0} = 148.0$ km/s, $\Omega_{ci0}^{-1} = 0.308$ s, and $T_0 = 228.32$ eV, where B_0 is the observed value of B_L recorded by TH-A at 2119:13 UT on the magnetosheath side of the current sheet (see Figure 5f). The

Table 3
LMN Dimensions and Maximum Variations of the Tripolar ΔB_M (nT) Out-of-Plane Magnetic Field on 15 November 2010 Relative to a Background Guide Magnetic Field $B_G = 15.9$ nT

Segment	Start (UT)	Δt (s)	$\Delta L, \Delta M, \Delta N$ (Li)	B_M (nT)	$\Delta B_M = B_M - B_G$ (nT)
TH-A $\Delta B_{M1} < 0$	2118:31.740	3.29	9.7, 0.8, −2.2	0.6	−15.3
TH-A $\Delta B_{Mc} > 0$	2118:35.030	14.97	44.1, 3.7, −10.1	39.7	+23.8
TH-A $\Delta B_{M2} < 0$	2118:50.000	9.40	27.7, 2.3, −6.3	−18.4 [−9.5]	−34.3 [−25.4]
TH-E $\Delta B_{M1} < 0$	2118:11.700	21.77	59.8, 6.5, −18.6	1.2	−14.7
TH-E $\Delta B_{Mc} > 0$	2118:33.470	9.04	24.8, 2.7, −7.7	34.1	+18.2
TH-E $\Delta B_{M2} < 0$	2118:42.510	9.54	26.2, 2.8, −8.2	−21.5 [−16.2]	−37.4 [−32.1]

Note. Dimensions, given in units of the ion inertial length $Li = 99.96$ km (see text), are based on time duration Δt (s) and LMN structure velocity $\mathbf{V}_{HT}$. The LMN structure velocity is $\mathbf{V}_{HT} = [294.77, 24.69, −67.51]$ km/s for TH-A and $\mathbf{V}_{HT} = [274.54, 29.69, −85.44]$ km/s for TH-E. B_M values stated in brackets are average values with peak B_M minima of Figures 5g and 5s excluded.

reference number density is arbitrary, not corresponding to any observed density, but chosen for numerical expediency.

The simulation results are displayed in the same boundary normal LMN coordinate system as used for the observations with positive **L** in the direction of the reconnecting magnetic field on the magnetospheric side, **N** in the normal direction from the magnetosphere to the magnetosheath, and $\mathbf{M} = \mathbf{N} \times \mathbf{L}$ being positive in the dawnward direction. The 2.5-D simulation, which employs periodic boundary conditions, is performed in the NL plane. The choice of periodic boundary conditions is a feature of the simulation that imposes a string of multiple active X-lines along the current sheet and a particle recirculation capable of mimicking injections from secondary X-lines. This allows a more direct test of the observations than using open boundary conditions. The ion to electron mass ratio $m_i/m_e = 25$ is sufficient to support Hall physics, and the normalized speed of light $c/c_{A0} = 30$. The physical size of the simulation domain is $L_L \times L_N = 204.8 \times 102.4\ d_{i0}$ with a uniform grid size of $0.0125\ d_{i0}$. There are initially 50 macroparticles per grid cell corresponding to a total of ~6.7×10^9 particles per species. Particles are weighted to have a uniform average number of particles per grid cell at the initial time. The particle time step $dt = 0.00125\ \Omega_{ci0}^{-1}$. The time step for the electromagnetic fields is dt/3 in order to resolve light waves.

The initial conditions consist of two oppositely directed current sheets. At time $t = 0$, the spatial profiles of the reconnecting B_L component and the out-of-plane B_M component of the magnetic field are given as

$$B_L(N) = \frac{B_{L,1} + B_{L,2}}{2} \left[\tanh\left(\frac{N - \frac{L_N}{4}}{w_0}\right) - \tanh\left(\frac{N - \frac{3L_N}{4}}{w_0}\right) + \tanh\left(\frac{N - \frac{5L_N}{4}}{w_0}\right) - \tanh\left(\frac{N + \frac{L_N}{4}}{w_0}\right) + 1 \right] + \frac{B_{L,1} - B_{L,2}}{2}$$

$$B_M(N) = \frac{B_{M,1} - B_{M,2}}{2} \left[\tanh\left(\frac{N - \frac{L_N}{4}}{w_0}\right) - \tanh\left(\frac{N - \frac{3L_N}{4}}{w_0}\right) + \tanh\left(\frac{N - \frac{5L_N}{4}}{w_0}\right) - \tanh\left(\frac{N + \frac{L_N}{4}}{w_0}\right) + 1 \right] + \frac{B_{M,1} + B_{M,2}}{2}$$

Table 4
LMN Dimensions of ΔB_M (nT) Variations on 15 November 2010 Relative to a Background Out-of-Plane Guide Magnetic Field $B_G = 8.6$ nT

Segment	Start (UT)	Δt (s)	$\Delta L, \Delta M, \Delta N$ (Li)	B_M (nT)	$\Delta B_M = B_M - B_G$ (nT)
TH-A $\Delta B_{M2} < 0$	2120:10.230	5.82	6.9, − 3.0, 10.8	−20.7	−29.3
TH-A $\Delta B_{Mc} > 0$	2120:16.050	23.10	27.4, − 11.9, 42.7	64.0	+55.4
TH-E $\Delta B_{M2} < 0$	2120:01.130	7.43	8.6, − 4.1, 13.0	−11.8	−20.4
TH-E $\Delta B_{Mc} > 0$	2120:08.565	13.32	15.4, − 7.4, 23.2	38.5	+29.9
TH-E $\Delta B_{M1} < 0$	2120:21.880	8.52	9.9, − 4.8, 14.9	−35.0	−43.6

Note. Dimensions, relative to the local ion inertial length $Li = 92.09$ km (see text), are based on time duration Δt (s) and LMN structure velocity $\mathbf{V}_{HT}$. The LMN structure velocity is $\mathbf{V}_{HT} = [109.38, −47.51, 170.17]$ km/s for TH-A and $\mathbf{V}_{HT} = [106.60, −51.38, 160.74]$ km/s for TH-E.

The spatial B_L and B_M profiles are equivalent to equations (8) and (9) of Malakit et al. (2010) aside from the addition of a guide field. The ion T_i and electron T_e temperature profiles at time $t = 0$ are identical to the spatial dependence of B_M. The asymptotic values on the magnetosphere side are denoted with subscripts "1" and those on the magnetosheath side are denoted with subscripts "2." The initial current sheet half-thickness $w_0 = 1.29\ d_{i0}$. The number density profiles are chosen so that total pressure balance is achieved in the fluid sense.

The goal is to achieve asymptotic plasma parameters on the two sides of the simulated current sheets that correspond to the THEMIS satellite observations. However, the event examined here introduces some ambiguity in achieving local pressure balance of the simulated current sheet as discussed briefly below. We use TH-A data at 2117:33 UT for the magnetosphere side and TH-A data at 2119:13 UT for the magnetosheath side (see Figure 5). The inferred magnetosheath parameters are $B_{L2}/B_0 = 1.000$, $B_{M2}/B_0 = 0.436$, $n_2/n_0 = 0.576$, $T_{i2}/T_0 = 1.069$, and $T_{e2}/T_0 = 0.262$. However, in using measured temperature moments of the entire ion distribution on the magnetosphere side, we find that the observed values are not consistent with local pressure balance in the fluid sense, which is expected in the physical system. In particular, the average ion temperature obtained by TH-A in the outer magnetosphere at 2117:30 UT suggests a relatively cold proton temperature of only 787 eV due to the presence of a cold ion population (see Figure 5a).

To address this, we set up two different simulations, each employing a different approach to attain pressure balance, and test whether the different approaches influence the results of importance for this study. The first assumption is to use observed data for all temperatures except for the electron temperature on the magnetospheric side, which is set to obtain pressure balance in the fluid sense. Using this assumption, the magnetospheric plasma parameters are $B_{L1}/B_0 = 1.377$, $B_{M1}/B_0 = 0.448$, $n_1/n_0 = 0.025$, $T_{i1}/T_0 = 3.448$, and $T_{e1}/T_0 = 8.865$. We note that the ratio of guide field to reconnecting field (B_{Mi}/B_{Li}, with $i = 1, 2$) on both sides of the current sheet is nearly the same, that is, about 0.4. However, these parameters result in an atypical $T_{e1} > T_{i1}$. The second assumption is to use measured T_{i2} and T_{e2}, while assuming a typical $T_{i1}/T_{e1} \sim 5$ ratio for the magnetosphere proper. All parameters are the same in the two simulations with the exception of the magnetospheric ion and electron temperatures, which are $T_{i1}/T_0 = 10.249$ and $T_{e1}/T_0 = 2.065$. We explore the effects of the two different magnetospheric temperature ratios on the out-of-plane B_M magnetic field evolution in a reduced domain size $L_L \times L_N = 102.4 \times 51.2\ d_{i0}$. A detailed comparison of B_M (not shown) reveals quite similar macroscale and mesoscale structures in the two simulations. Furthermore, ion velocity distributions in representative locations from both simulations are qualitatively similar (not shown). We conclude that, for the purpose of the present study, using the first assumption with an atypical ion to electron temperature ratio on the magnetospheric side does not seem to adversely affect the interpretation of our results. Thus, in what follows, we strictly show results from the larger domain simulation with parameters given by the first assumed profile with $T_{e1} > T_{i1}$.

Reconnection is initiated in the simulation by coherently perturbing the in-plane magnetic field with an amplitude $0.025B_0$ in B_N and B_L to generate an X-line/O-line pair at both current sheets. As the simulation evolves in time the initial O-lines, that is, the primary magnetic islands, grow mainly along the inflow (N) direction, and secondary magnetic islands are generated. The secondary islands either merge with one another to form bigger islands, or they drift away from the main X-line and eventually merge with the primary island. Our simulation is carried out until $t = 80\ \Omega_{ci0}^{-1}$. This is long after the reconnection rate reaches a quasi steady state at around $t = 25\ \Omega_{ci0}^{-1}$ (not shown). We first explore the out-of-plane magnetic fields at the end of the simulation, that is, at $t = 80\ \Omega_{ci0}^{-1}$. All simulation results are presented for the current sheet in the region $0 \leq N \leq L_N/2$ of the simulation domain.

4.2. Macroscopic PIC Simulation Results

Figure 10a shows the out-of-plane guide magnetic field B_M in the NL plane relative to a background guide field $B_G/B_0 \sim 0.4$ in the positive M direction (dawnward). Red colors correspond to $\Delta B_M > 0$ (dawnward variations) and blue colors correspond to $\Delta B_M < 0$ (duskward variations). The in-plane magnetic field is depicted as black solid lines with a positive (northward) B_L component at $N - N_{XL} < 0$ and a negative (southward) B_L at $N - N_{XL} > 0$, with distances in the NL plane measured relative to the primary X-line location at $(L_{XL}, N_{XL}) = (138.95, 25.55)\ d_{i0}$. A black dashed line marks the spatial location where $B_L = 0$. The associated out-of-plane current flows in the negative M direction, antiparallel to the guide field direction, as in the
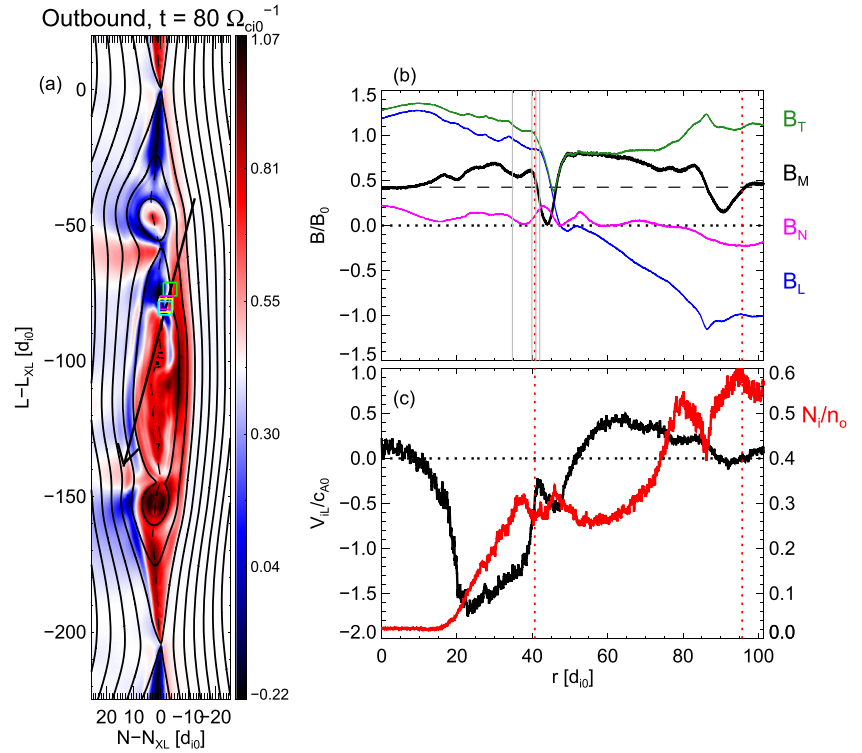
Figure 10. (a) The out-of-plane B_M component of the magnetic field from the PIC simulation at time $t = 80 \, \Omega_{cio}^{-1}$ with positive (dawnward) changes in red and negative (duskward) changes in blue relative to a dawnward ($B_G/B_L = 0.42$) guide field. The in-plane (NL plane) magnetic field lines are shown as black solid lines. A black dashed line marks $B_L = 0$. The low-density magnetosphere is at negative $N - N_{XL}$ values, and the high-density magnetosheath is at positive $N - N_{XL}$ values. (b) Magnetic field components (B_L = blue, B_M = black, B_N = magenta) and total magnetic field strength (B_T = green) along the outbound, oblique virtual satellite trajectory indicated in Panel (a). (c) Ion number density N_i (red) and L component of the ion velocity Vi_L (black) along the same outbound trajectory. Horizontal axes of Panels (b) and (c) display the along-track distance r with $r = 0$ at the start of the cut. Red vertical dotted lines bracket tripolar B_M intervals. Four colored square symbols along the outbound trajectory in Panel (a) mark a series of four locations where the ion VDFs of Figure 11 are measured. Panel (b) marks the same ion VDF locations as four vertical solid lines in gray color. The region illustrated in the L direction exceeds the size of the computational domain; periodic boundary conditions are used to extend the plot region to contain two active X-lines.

THEMIS observations reported in sections 2 and 3. The low-density magnetosphere is in the $N - N_{XL} < 0$ region, and the high-density magnetosheath is located at $N - N_{XL} > 0$.

In this periodic system, the primary X-line at $L - L_{XL} = 0$ is also located at $-204.8 \, d_{i0}$, such that they bracket a primary magnetic island. There are also recently formed secondary islands at $L - L_{XL} = -50$ and $-150 \, d_{i0}$. To compare the numerical signatures with THEMIS observations, we obtain an outward, oblique cut through the primary island at a 15° average angle relative to the L direction as inferred observationally from the deHoffmann-Teller structure velocity of the first, outbound MP crossing in section 3. A crossing at this oblique angle is depicted by the black arrow from the magnetosphere to the magnetosheath in Figure 10a.

The magnetic field and the plasma properties are obtained along this virtual path through the simulation. Figure 10b shows the magnetic field components (B_L is blue, B_M is black, and B_N is magenta) and total strength B_T (in green) for the outbound trajectory. Figure 10c shows the corresponding ion velocity component Vi_L along the outflow direction and the ion plasma number density N_i. All parameters are plotted as a function of r, defined as the distance along the trajectory relative to its starting point in units of d_{i0}.

The virtual spacecraft path shown in Figure 10a pierces the primary magnetic island. As it passes from the magnetospheric side ($N - N_{XL} < 0$) to the magnetosheath side ($N - N_{XL} > 0$) of the current sheet, a region with a positive ΔB_M enhancement is seen up to $r \sim 40 \, d_{i0}$. Subsequently, a tripolar ΔB_M signature is present with a negative perturbation at $40 < r < 47 \, d_{i0}$, followed by a positive perturbation at $47 < r < 86 \, d_{i0}$, and

finally a second, negative ΔB_M perturbation at $86 < r < 95\ d_{i0}$. During this tripolar variation, the ion outflow velocity Vi_L (Figure 10c) transitions from a more negative value on the magnetospheric side ($B_L > 0$) to a positive value on the magnetosheath side ($B_L < 0$). This resembles the bidirectional jet recorded by TH-A during its outbound MP crossing with a more intense northward ($Vi_L > 0$) jet toward the magnetosheath as observed in the satellite frame of reference and shown in Figure 5i and Figure 9c. The initial simulated ΔB_M enhancement and the subsequent tripolar field perturbation display a remarkable similarity with those observed by TH-A and TH-E (see Figures 5g and 5s) during their outbound MP crossings.

The maximum $\Delta B_M = |B_M - B_G|$ value in each part of the simulated tripolar variation divided by the simulation guide field value ($B_G = 0.4$) results in $\Delta B_{M1}/B_G = 0.96$, $\Delta B_{Mc}/B_G = 1.03$, and $\Delta B_{M2}/B_G = 0.62$, where subscripts "1" (magnetosphere side), "c" (core field), and "2" (magnetosheath side) refer to the same regions as listed in Table 3. The corresponding values for the observations, using the values presented in Table 3, are $\Delta B_{M1}/B_G = 0.96$ (0.92), $\Delta B_{Mc}/B_G = 1.50$ (1.14), and $\Delta B_{M2}/B_G = 1.60$ (2.02) for TH-A (TH-E) observations, where $B_G = 15.9$ nT. The simulated variations ΔB_{M1} and ΔB_{Mc} agree reasonably well with the observations. The $\Delta B_{M2}/B_G$ variation, however, is lower in the simulation on the magnetosheath side of the current sheet than THEMIS observed by a factor of 2.6 for TH-A and by a factor of 3.3 for TH-E, if we exclude the few data points around the extreme B_M minima shown in Figures 5g and 5s. Figures 5e–5g confirm that the very local B_M minimum that TH-A observed on the $B_L < 0$ side of the MP boundary layer is associated with an additional, highly localized $B_L < 0$ enhancement just before 2119:00 UT that resulted in a further compression of the total magnetic field strength than what we already discussed in section 2 for the magnetic field on this side of the MP. It is possible that some of the differences between the observed and simulated B_M depression on this magnetosheath side is due to a dynamic draping of magnetosheath fields around a bulging magnetic field structure that may have been more severe at the actual MP than what this stand-alone PIC simulation can reproduce in which reconnection is initiated using a perturbed magnetic field with no external magnetic field draping. Nevertheless, the exceptional overall agreement of the simulated and observed parameters along this outbound crossing, as illustrated in Figures 9 and 10, including a localized depression of the total magnetic field around $B_L = 0$, provide strong supporting evidence that THEMIS encountered an early-stage, crater-like nascent flux rope between two active reconnection X-lines at the dayside MP current sheet.

The observed spatial dimensions of the outbound tripolar magnetic field signature are also comparable to those of the simulation. The along-track dimension of the simulated tripolar signature is obtained as the distance $r = 55.1\ d_{i0}$ between the pair of vertical red dotted lines in Figure 10b. Here, $d_{i0} = 45.54$ km, so $r = 2{,}509$ km. The spatial dimension of the observed tripolar signature was presented in section 3 in terms of the ion inertial length Li scale based on the average ion density across the entire signature. The average ion density across the complete spatial extent of the simulated tripolar signature, as obtained between the pair of vertical dotted lines in Figure 10b, is $N_{i,avg}/n_0 = 0.3753$ ($N_{i,avg} = 9.38$ cm^{-3}). That is, $Li = 74.34$ km $\sim 1.63\ d_{i0}$ and the along-track dimension of the simulated tripolar signature is $2{,}509$ km/74.34 km $\sim 33.8\ Li$ in terms of this average structure density. The cumulative sum of each consecutive ΔL displacement (cf. fourth column of Table 3) of the observed tripolar field variation results in a total $\Delta L = 81.5\ Li$ for TH-A and $\Delta L = 110.8\ Li$ for TH-E. Similarly, the total displacement along the normal direction is $\Delta N = -18.6\ Li$ and $\Delta N = -34.5\ Li$ for TH-A and TH-E, respectively. Thus, the observed along-track dimension of the tripolar signature is $(\Delta L^2 + \Delta N^2)^{1/2}$, or $83.6\ Li$ for TH-A and $116.0\ Li$ for TH-E. These NL plane distances correspond to $8{,}356$ km for TH-A and $11{,}600$ km for TH-E, where $Li = 99.96$ km. The in-plane dimension of the simulated tripolar signature is a factor of ~ 3.3–4.6 smaller than the observed tripolar signature.

4.3. Microscopic PIC Simulation Results

To explore the proposed link between a tripolar ΔB_M magnetic field signature and a presence of two active X-lines, we investigate ion VDFs in the numerical simulation, specifically surveying the distributions for evidence of the type of counterpropagating ion beams that THEMIS measured at the dayside MP current sheet on 15 November 2010. Figure 11 displays four simulated ion VDFs in the same field-aligned coordinate system as discussed for the THEMIS ion VDFs of Figures 6 and 7. The simulated ion distributions are numbered in the spatial sequence shown by both the colored symbols along the outbound trajectory of Figure 10a and the vertical gray lines in Figure 10b. Ion VDF #1 shows a southward ($-L$ directed) ion
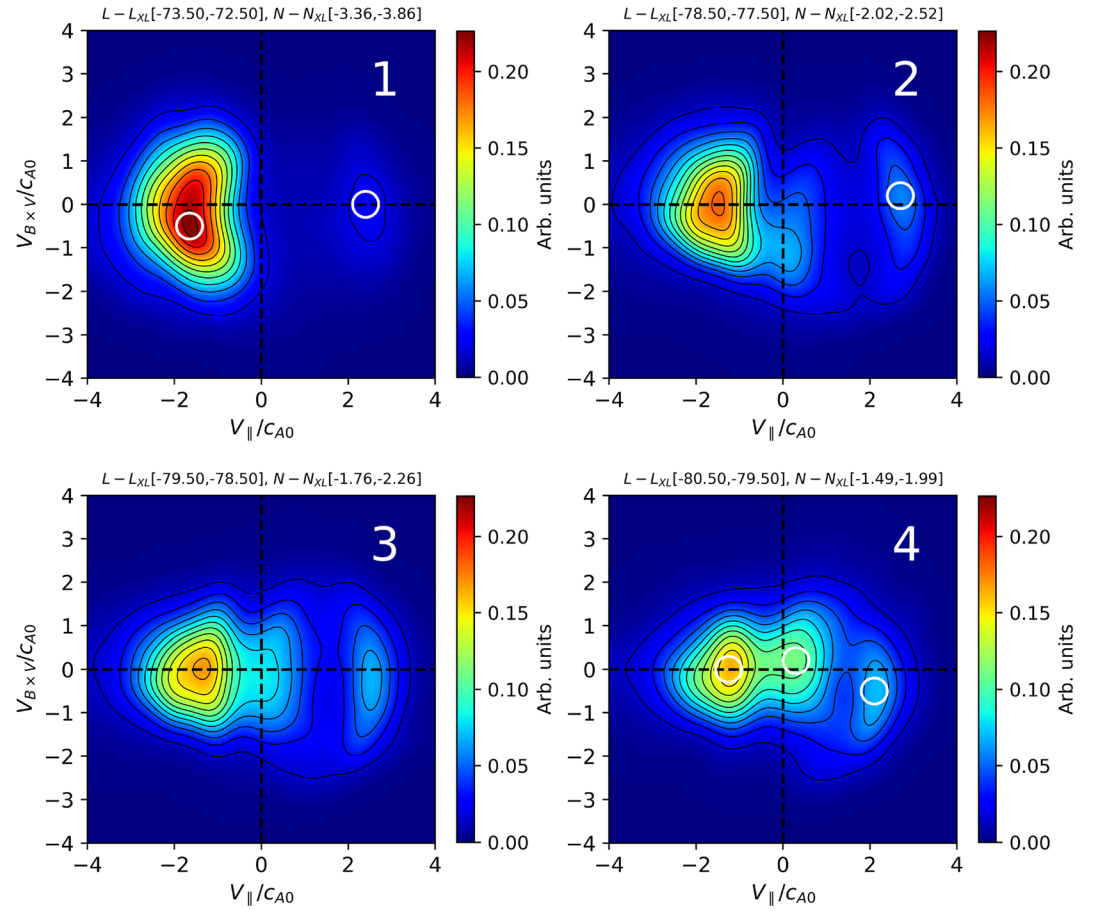
Figure 11. Four ion VDFs (1–4) obtained at four locations along the outbound trajectory of Figure 10a, where VDF #1 = green, #2 = magenta, #3 = yellow, and #4 = cyan. Each ion VDF is acquired in a rectangular region noted on top of each panel with $[N \times L]$ dimension of $[0.5 \times 1.0]\, d_{i0}$. Ion velocities are rotated into a local magnetic field-aligned coordinate system and projected into the $(V_{\parallel} \times V_{\mathrm{B} \times \mathrm{V}})/c_{\mathrm{A0}}$ space to generate VDFs in the same format that THEMIS ion VDFs employ, where $c_{\mathrm{A0}} = 148$ km/s is the ion Alfvén speed based on the reference magnetic field $B_0 = 33.9$ nT and plasma number density $n_0 = 25$ cm^{-3}. White circles indicate the $0.3\, c_{\mathrm{A0}}$ radius of velocity space from which positively charged macroparticles are taken to explore a representative space-time history (see text for details).

beam. The phase space density of this beam decreases as the virtual satellite approaches the current sheet from ion VDF #1 to #3, while the phase space density of the northward ($+L$ directed) ion beam increases from ion VDF #1 to #3. The spatial sequence of the simulated ion VDFs #1, #2, and #3 along the outbound trajectory thus displays a remarkable similarity with the velocity space evolution of the ion VDFs that TH-A measured on this same $B_{\mathrm{L}} > 0$ earthward side of the current sheet (see Figures 6c–6e) as it traversed a crater-like nascent flux rope. The three simulated ion VDFs and the three measured ion VDFs were all recorded just earthward of the peak LLBL side B_{M} depression of the outbound tripolar B_{M} perturbation. The three populations of the simulated ion VDF #4 as recorded on this $B_{\mathrm{L}} > 0$ side of the nascent flux rope are also reminiscent of the ion VDF that TH-E sampled at 2120:06 UT (see Figure 7b) on the $B_{\mathrm{L}} < 0$ magnetosheath side of the inbound FTE flux rope crossing. The two simulated ion VDFs #3 and #4, which are recorded closer to the location where $B_{\mathrm{L}} = 0$, display a more circular, antiparallel velocity distribution as compared with the clearly "D-shaped," antiparallel distributions simulated farther earthward of $B_{\mathrm{L}} = 0$ in ion VDFs #1 and #2, which are typically expected in ion exhaust flows (e.g., Cowley, 1982).

To investigate whether the presence of counterpropagating ion beams in the PIC simulation is a signature of multiple X-lines, we follow the self-consistent time evolution of two representative ions from each of the encircled populations in Figure 11. These ions are macroparticles that self-consistently evolve during the
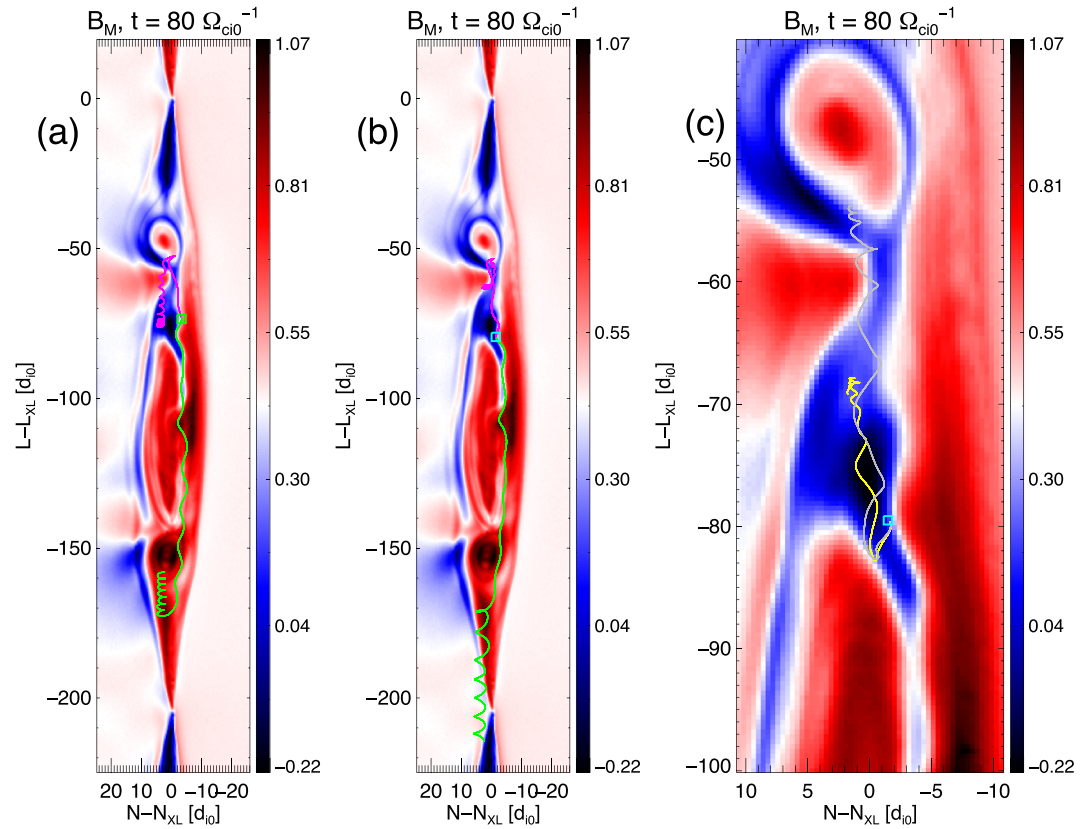
Figure 12. Ion trajectories from representative particles within the encircled beams of the simulated ion VDFs presented in Figure 11. Trajectories are superposed on the simulated out-of-plane magnetic field B_M at time $t = 80 \, \Omega_{ci0}^{-1}$. Spatial coordinates are the same as in Figure 10a: (a) particle trajectories of two representative ions from the antiparallel beam (magenta) and the parallel beam (green) of ion VDF #1; (b) particle trajectories of two representative ions from the antiparallel beam (magenta) and the faster parallel beam (green) of ion VDF #4; (c) particle trajectories of two representative ions of the slower, parallel-propagating population in ion VDF #4.

simulation from the initial time $t = 0$, that is, they are not "test particles." Figure 12 shows the trajectories of these particles superposed on B_M at simulation time $t = 80 \, \Omega_{ci0}^{-1}$. Figure 12a presents two ion trajectories, one from each of the two encircled beams in VDF #1. This VDF is sampled at the location marked by a green-colored open-square symbol. A magenta-colored trace corresponds to the time evolution of the particle in the antiparallel ion beam. The green trace corresponds to the time history of the parallel-propagating ion beam. Figure 12b shows the representative time histories of the encircled antiparallel ion beam (magenta trace) and the faster, parallel-propagating ions (green trace) of VDF #4. This VDF #4 is measured at the location of the cyan-colored square symbol. Figure 12c shows a close-up region with two particle trajectories (gray and yellow traces) from the encircled slower, parallel-propagating ion beam in VDF #4 of Figure 11. We first discuss results for the antiparallel-propagating ion beams, and then describe those for the parallel-propagating ion beams.

The representative particle trajectories for the antiparallel ion beams, as shown by the magenta-colored curves in Figures 12a and 12b, indicate that they originate from the dense magnetosheath. They are located in the $-80 < L - L_{XL} < -60 \, d_{i0}$ range at $t = 0$. Both ions initially move northward, that is, toward positive L. At $t = 56 \, \Omega_{ci0}^{-1}$, they approach the current sheet and eventually enter the southward ($-L$ directed) exhaust region near the X-line bounding the secondary island, which is centered at $L - L_{XL} = -50 \, d_{i0}$ at $t = 80 \, \Omega_{ci0}^{-1}$. When the particles enter this southward exhaust, they begin to gyrate about the newly reconnected field lines. The guiding center motion thus experiences a turning point, where the initially northward directed magnetosheath ions turn southward and start moving opposite to the magnetospheric ($B_L > 0$) field.

Particles from the parallel-propagating beams in ion VDF #1 (Figure 12a), and ion VDF #2 (not shown), move southward, but otherwise behave in a qualitatively similar manner to those in the antiparallel-propagating beams. With the exception of particles in the slower, parallel-propagating beam in ion VDF #4 (Figure 12c), a common feature of all representative macroparticles belonging to the parallel ion beams is that they enter the exhaust region of the X-line to the north of a secondary magnetic island around simulation time $t = 40\ \Omega_{ci0}^{-1}$ when that X-line was located near $L - L_{XL} = -178\ d_{i0}$. As the simulation progresses, the X-line drifts northward to $L - L_{XL} = -145\ d_{i0}$ at $t = 80\ \Omega_{ci0}^{-1}$ (see Figures 12a and 12b). As the particles enter the exhaust region, their Larmor trajectories change appreciably and they all end up drifting northward along magnetospheric ($B_L > 0$) magnetic field lines after $t = 40\ \Omega_{ci0}^{-1}$ until they reach the locations where we measure the parallel beams of these ion VDFs.

The time histories of the two slower, parallel-propagating ions of VDF #4, as shown in Figure 12c, are both closer to the center of the current sheet than the other particle trajectories of Figure 12. As the simulation progresses, the slow ion with a gray-colored trajectory crosses the current sheet a number of times. Moreover, both ions move southward toward the middle of the primary magnetic island and it is not until $t = 72\ \Omega_{ci0}^{-1}$ that their guiding center motion turns northward. This northward change of the gyro-orbit is due to an in-plane electric field (not shown) acting on the slow ion particles, rather than due to any proximity to the exhaust region near an X-line as is the case with the particles of the faster ion beams.

In summary, the simulated ion VDFs along with the representative macroparticle evolution from the antiparallel ion beams and the faster, parallel-propagating ion beams in this PIC simulation provide additional evidence that the counterpropagating ion beams observed by THEMIS are associated with two different X-lines.

5. Discussion

A configuration of multisatellite THEMIS observations is explored together with a dedicated PIC simulation of asymmetric magnetic reconnection to address the early-stage formation of a crater FTE flux rope, and the question of how multiple X-lines may generate a tripolar ΔB_M perturbation across the dayside asymmetric MP. The combined results displayed in Figures 9 and 10 together with observations and simulations of counterpropagating ion beams (cf. Figures 6 and 7 and Figure 11) confirm that a tripolar guide magnetic field can develop across a nascent flux rope at the dayside MP in the presence of two reconnection X-lines. The PIC simulation visualization of a tripolar B_M perturbation to the guide magnetic field suggests that it is due to a complicated interaction of the magnetosheath side Hall magnetic fields that emanate from each of two dominant X-lines that bracket an early-stage primary magnetic island. This Hall magnetic field is sometimes referred to as the unipolar Hall magnetic field rather than a quadrupole Hall magnetic field at the dayside asymmetric MP current sheet, since the Hall magnetic field of opposite polarity on the earthward side of the current sheet is significantly suppressed. In fact, it is barely noticeable in the results of this PIC simulation of asymmetric magnetic reconnection.

A steady northward magnetosheath flow, the positive-then-negative sense of the bipolar B_N magnetic field of the mature FTE, the northward drifts of the deHoffmann-Teller frames, the high-latitude TH-A position at $Z_{GSM} = 3.8\ R_E$ and the time sequence of a southward jet followed by a northward jet clearly show that TH-A traversed a northward drifting region of converging exhausts between two X-lines at the first MP current sheet rather than a jet reversal region of a single, southward drifting X-line. Two active X-lines at the dayside MP also explain the presence of two counterstreaming magnetosheath ion beams in a $B_L > 0$ region of the LLBL between the two opposite flow enhancements.

The classic D-shaped ion distributions discussed by Cowley (1982) display a low-energy Alfvén speed cutoff on the same side of $V_{||} = 0$ as the core of the magnetosheath population, whereas the D-shaped ion VDFs of Figure 6 often indicate a distribution that encircles $V_{||} = 0$. This distribution may be consistent with a magnetosheath population that first entered the magnetosphere across a set of open field lines due to a reconnection X-line to the north of the satellite, which is being driven northward by the fast magnetosheath flow and against the southward directed field line tension.

The higher phase space density of the antiparallel (southward) ion beam and the lower phase space density of the parallel (northward) ion beam at 2118:27 UT and 2118:30 UT (see Figures 6c and 6d) may be explained

in terms of the different distances these magnetosheath ions had to travel from each X-line to the observing TH-A satellite. There may be fewer ion particles in a given location with distance from the X-line as these jet-associated particles from the magnetosheath spread out in space. This result is supported by a particle tracing of two simulated ion macroparticles taken from two ion beams of VDF #1 that displayed a similarly different phase space density (cf. Figure 11) near the poleward X-line and the time history of their particle trajectories (cf. Figure 12a). The ion VDFs thus suggest that the more poleward TH-A satellite was close to a northern X-line at 2120:12 UT when it observed a fast, D-shaped, parallel (southward) ion beam (see Figure 6h) in a draped $B_L < 0$ field adjacent to the mature FTE flux rope. The counterstreaming antiparallel (northward) and parallel (southward) ion beams as measured by the equatorward TH-E satellite at 2120:06 UT (see Figure 7b) in a similarly draped $B_L < 0$ field adjacent to the mature FTE indicate that TH-E was closer to a southern X-line than TH-A at approximately the same time. The ion VDFs measured by TH-A and TH-E thus provide evidence that two X-lines were present during the first, outbound MP crossing associated with converging exhausts, enhanced total pressure at TH-A, substantial tripolar B_M perturbations, and a locally weaker total magnetic field B at the location where $B_L = 0$. The ion VDFs also suggest there are two X-lines across the subsequent mature FTE flux rope, which is associated with substantial increases of total pressure at both satellites, a tripolar B_M along the TH-E trajectory, and the highly asymmetric bipolar B_M across the FTE flux rope at TH-A. Finally, pitch angle observations of 2–5 keV magnetospheric electrons of Figure 3d support a presence of open field lines across both MP boundary layers in agreement with newly reconnected field lines.

The good agreement between THEMIS observations and the PIC simulation along the outbound crossing suggests that the initial dawnward ($\Delta B_M > 0$) enhancement deep within the LLBL region, and earthward of a tripolar ΔB_M field around $B_L = 0$, may be associated with a unipolar Hall magnetic field that extends northward from a southern X-line. The tripolar ΔB_M perturbations of substantial magnitudes as observed by THEMIS appear to be a consequence of a duskward ($\Delta B_M < 0$) unipolar Hall magnetic field that extends southward from a northern X-line that wraps around a region of a unipolar, dawnward Hall magnetic field that extends northward from a primary southern X-line. We interpret this dawnward $\Delta B_M > 0$ Hall magnetic field as the developing core field region of a nascent crater-like FTE flux rope.

6. Summary and Conclusions

THEMIS satellite observations from two nearby locations as recorded across two consecutive encounters of the asymmetric, northern dayside MP current sheet provide direct evidence that link a presence of substantial tripolar ΔB_M out-of-plane perturbations across the $B_L = 0$ current sheet with two active X-lines and the early, nascent stage of FTE flux rope formation.

We demonstrated that THEMIS traversed two different stages of flux rope formation associated with reconnection at the dayside asymmetric MP current sheet. The interpretation that THEMIS crossed a flux rope in its nascent stage of formation is supported by a dedicated 2-D PIC simulation of magnetic reconnection that produced remarkable agreement with the out-of-plane ΔB_M perturbations and exhaust directions that THEMIS observed across an outbound MP current sheet associated with a modest total pressure enhancement of a northward moving "crater-like" FTE with a noticeable depression of the total magnetic field strength near $B_L = 0$. The PIC simulation indicates that both B_M depressions of the tripolar ΔB_M observed across a nascent flux rope are due to a duskward ($\Delta B_M < 0$) Hall magnetic field on the magnetosheath side of the MP and associated with a northern X-line. The simulation strongly suggests that the dawnward ($\Delta B_M > 0$) core field section of the tripolar B_M perturbation that THEMIS recorded across the $B_L = 0$ region is associated with a dominant Hall field protruding northward from a southern X-line.

Within 70 s of the nascent flux rope encounter, TH-A observed a northward drifting mature FTE flux rope with a significant core field enhancement along the direction of the external guide field, while TH-E observed substantial magnitudes of another tripolar B_M perturbation relative to a weaker guide magnetic field as the two THEMIS satellites moved earthward across $B_L = 0$ at a separation distance of only 0.38 R_E. The sense of the tripolar B_M perturbation across this second inbound MP is identical to that of the earlier outbound MP crossing suggesting that this guide field perturbation is similar in nature to that observed across the nascent flux rope.

We propose, on the basis of a weaker external $B_G = 8.6$ nT guide field adjacent to a strong FTE flux rope and a stronger $B_G = 15.9$ nT external guide field adjacent to a nascent crater-like flux rope, that the core field of the FTE flux rope most likely developed as part of a growing Hall magnetic field along the guide field parallel direction near the $B_L = 0$ transition of the current sheet as magnetic flux accumulates in the exhaust convergence region between two active X-lines (e.g., Chen et al., 2017; Karimabadi et al., 1999).

Two counterstreaming ion beams of the observed ion VDFs in the exhaust convergence zone earthward of $B_L = 0$, and the corresponding ion VDFs from a 2-D numerical PIC simulation in very similar locations relative to the current sheet, provide direct support for the presence of two active X-lines across a nascent, crater-like FTE flux rope. A D-shaped southward ion beam from a northern X-line in a $B_L < 0$ region and northward exhausts on the $B_L > 0$ side of the MP current sheet from a southern X-line support the presence of two active X-lines across the mature FTE flux rope observed by TH-A. Two counterpropagating ion beams with low phase space density observed simultaneously with a third, slowly northward drifting magnetosheath ion population with high phase space density, as measured by TH-E within a $\Delta B_M < 0$ depression of a tripolar ΔB_M region on the magnetosheath $B_L < 0$ side of the MP layer, provide further evidence of two active X-lines at the time of the mature FTE flux rope. A similar ion VDF with three distinct ion populations is produced on the magnetosphere $B_L > 0$ side of the MP current sheet in a 2-D PIC simulation of a nascent crater-like primary magnetic island associated with a tripolar ΔB_M signature. Trajectories of some representative positively charged macroparticles as measured in two counterpropagating beams of the simulated ion VDFs show that they are associated with the exhaust regions of two different X-lines. Further research is required into observed and simulated ion VDFs near multiple reconnection X-lines to understand how common this type of ion VDF with three distinct populations may be, and whether it is unique to regions between two active X-lines.

Data Availability Statement

THEMIS observations can be found at http://themis.ssl.berkeley.edu/index.shtml and from the NASA CDAWeb heliophysics repository. THEMIS energy-time spectrograms and ion VDFs were processed using SPEDAS V3.1 as described by Angelopoulos et al. (2019). ACE observations and 1 min OMNI solar wind data were obtained from the NASA CDAWeb (at https://cdaweb.gsfc.nasa.gov). *P3D* PIC simulation data used to generate the simulation figures can be obtained online (at https://doi.org/10.5281/zenodo.3631824).

References

Angelopoulos, V. (2008). The THEMIS mission. *Space Science Reviews*, *141*(1–4), 5–34. https://doi.org/10.1007/s11214-008-9336-1

Angelopoulos, V., Cruce, P., Drozdov, A., Grimes, E. W., Hatzigeorgiu, N., King, D. A., et al. (2019). The Space Physics Environment Data Analysis System (SPEDAS). *Space Science Reviews*, *215*(1), 9. https://doi.org/10.1007/s11214-018-0576-4

Auster, H. U., Glassmeier, K.-H., Magnes, W., Aydogar, O., Baumjohann, W., Constantinescu, D., et al. (2008). The THEMIS fluxgate magnetometer. *Space Science Reviews*, *141*(1–4), 235–264. https://doi.org/10.1007/s11214-008-9365-9

Birdsall, C. K., & Langdon, A. B. (2004). *Plasma physics via computer simulation*. London: Taylor & Francis.

Birn, J., Borovsky, J. E., & Hesse, M. (2008). Properties of asymmetric magnetic reconnection. *Physics of Plasmas*, *15*(3), 32,101-1–32,101-13. https://doi.org/10.1063/1.2888491

Birn, J., Drake, J. F., Shay, M. A., Rogers, B. N., Denton, R. E., Hesse, M., et al. (2001). Geospace Environmental Modeling (GEM) magnetic reconnection challenge. *Journal of Geophysical Research*, *106*(A3), 3715–3719. https://doi.org/10.1029/1999JA900449

Burch, J. L., Torbert, R. B., Phan, T. D., Chen, L. J., Moore, T. E., Ergun, R. E., et al. (2016). Electron-scale measurements of magnetic reconnection in space. *Science*, *352*(6290). https://doi.org/10.1126/science.aaf2939

Cassak, P. A., & Shay, M. A. (2007). Scaling of asymmetric magnetic reconnection: General theory and collisional simulations. *Physics of Plasmas*, *14*(10), 102114. https://doi.org/10.1063/1.2795630

Chen, Y., Tóth, G., Cassak, P. A., Jia, X., Gombosi, T. I., Slavin, J. A., et al. (2017). Global three-dimensional simulation of Earth's dayside reconnection using a two-way coupled magnetohydrodynamics with embedded particle-in-cell model: Initial results. *Journal of Geophysical Research: Space Physics*, *122*, 10,318–10,335. https://doi.org/10.1002/2017JA024186

Cowley, S. W. H. (1982). The causes of convection in the Earth's magnetosphere: A review of developments during the IMS. *Reviews of Geophysics and Space Physics*, *20*(3), 531–565. https://doi.org/10.1029/RG020i003p00531

Daldorff, L. K. S., Tóth, G., Gombosi, T. I., Lapenta, G., Amaya, J., Markidis, S., & Brackbill, J. U. (2014). Two-way coupling of a global Hall magnetohydrodynamics model with a local implicit particle-in-cell model. *Journal of Computational Physics*, *268*, 236–254. https://doi.org/10.1016/j.jcp.2014.03.009

Daly, P. W., Williams, D. J., Russell, C. T., & Keppler, E. (1981). Particle signature of magnetic flux transfer events at the magnetopause. *Journal of Geophysical Research*, *86*(A3), 1628–1632. https://doi.org/10.1029/JA086iA03p01628

Dorelli, J. C., & Bhattacharjee, A. (2009). On the generation and topology of flux transfer events. *Journal of Geophysical Research*, *114*, A06213. https://doi.org/10.1029/2008JA013410

Dungey, J. W. (1961). Interplanetary magnetic field and the auroral zones. *Physical Review Letters*, *6*(2), 47–48. https://doi.org/10.1103/PhysRevLett.6.47

Eriksson, S., Cassak, P. A., Retinò, A., & Mozer, F. S. (2016). Subsolar magnetopause observation and kinetic simulation of a tripolar guide magnetic field perturbation consistent with a magnetic island. *Geophysical Research Letters*, *43*, 3035–3041. https://doi.org/10.1002/2016GL068691

Eriksson, S., Lapenta, G., Newman, D. L., Phan, T. D., Gosling, J. T., Lavraud, B., et al. (2015). On multiple reconnection X-lines and tri-polar perturbations of strong guide magnetic fields. *Astrophysics Journal*, *805*(1), 43. https://doi.org/10.1088/0004-637X/805/1/43

Eriksson, S., Newman, D. L., Lapenta, G., & Angelopoulos, V. (2014). On the signatures of magnetic islands and multiple X-lines in the solar wind as observed by ARTEMIS and WIND. *Plasma Physics and Controlled Fusion*, *56*(6), 064008. https://doi.org/10.1088/0741-3335/56/6/064008

Escoubet, C. P., Fehringer, M., & Goldstein, M. (2001). The Cluster mission. *Annales Geophysicae*, *19*(10/12), 1197–1200. https://doi.org/10.5194/angeo-19-1197-2001

Fuselier, S. A., Petrinec, S. M., Trattner, K. J., Broll, J. M., Burch, J. L., Giles, B. L., et al. (2018). Observational evidence of large-scale multiple reconnection at the Earth's dayside magnetopause. *Journal of Geophysical Research: Space Physics*, *123*, 8407–8421. https://doi.org/10.1029/2018JA025681

Gosling, J. T., Skoug, R. M., McComas, D. J., & Smith, C. W. (2005). Direct evidence for magnetic reconnection in the solar wind near 1 AU. *Journal of Geophysical Research*, *110*, A01107. https://doi.org/10.1029/2004JA010809

Hapgood, M. A. (1992). Space physics coordinate transformations: A user guide. *Planetary and Space Science*, *40*(5), 711–717. https://doi.org/10.1016/0032-0633(92)90012-D

Hasegawa, H., Wang, J., Dunlop, M. W., Pu, Z. Y., Zhang, Q.-H., Lavraud, B., et al. (2010). Evidence for a flux transfer event generated by multiple X-line reconnection at the magnetopause. *Geophysical Research Letters*, *37*, L16101. https://doi.org/10.1029/2010GL044219

Hoilijoki, S., Ganse, U., Sibeck, D. G., Cassak, P. A., Turc, L., Battarbee, M., et al. (2019). Properties of magnetic reconnection and FTEs on the dayside magnetopause with and without a positive IMF *Bx* component during southward IMF. *Journal of Geophysical Research: Space Physics*, *124*, 4037–4048. https://doi.org/10.1029/2019JA026821

Karimabadi, H., Krauss-Varban, D., Omidi, N., & Vu, H. X. (1999). Magnetic structure of the reconnection layer and core field generation in plasmoids. *Journal of Geophysical Research*, *104*(A6), 12,313–12,326. https://doi.org/10.1029/1999JA900089

Khrabrov, A. V., & Sonnerup, B. U. Ö. (1998). DeHoffmann-Teller analysis. In G. Paschmann, & P. W. Daly (Eds.), *Analysis methods for multi-spacecraft data* (pp. 221–248). Noordwijk, Netherlands: European Space Agency Publications Division.

King, J. H., & Papitashvili, N. E. (2005). Solar wind spatial scales in and comparisons of hourly Wind and ACE plasma and magnetic field data. *Journal of Geophysical Research*, *110*, A02104. https://doi.org/10.1029/2004JA010649

LaBelle, J., Treumann, R. A., Haerendel, G., Bauer, O. H., Paschmann, G., Baumjohann, W., et al. (1987). AMPTE IRM observations of waves associated with flux transfer events in the magnetosphere. *Journal of Geophysical Research*, *92*(A6), 5827–5843. https://doi.org/10.1029/JA092iA06p05827

Lee, L.-C., & Fu, Z.-F. (1985). A theory of magnetic flux transfer at the Earth's magnetopause. *Geophysical Research Letters*, *12*(2), 105–108. https://doi.org/10.1029/GL012i002p00105

Malakit, K., Shay, M. A., Cassak, P. A., & Bard, C. (2010). Scaling of asymmetric magnetic reconnection: Kinetic particle-in-cell simula-tions. *Journal of Geophysical Research*, *115*, A10223. https://doi.org/10.1029/2010JA015452

Mandt, M. E., Denton, R. E., & Drake, J. F. (1994). Transition to whistler mediated magnetic reconnection. *Geophysical Research Letters*, *21*(1), 73–76. https://doi.org/10.1029/93GL03382

McFadden, J. P., Carlson, C. W., Larson, D., Ludlam, M., Abiad, R., Elliott, B., et al. (2008). The THEMIS ESA plasma instrument and in-flight calibration. *Space Science Review*, *141*(1–4), 277–302. https://doi.org/10.1007/s11214-008-9440-2

Mozer, F. S., Bale, S. D., & Phan, T. D. (2002). Evidence of diffusion regions at a subsolar magnetopause crossing. *Physical Review Letters*, *89*(1), 15,002-1–15,002-4. https://doi.org/10.1103/PhysRevLett.89.015002

Owen, C. J., Marchaudon, A., Dunlop, M. W., Fazakerley, A. N., Bosqued, J.-M., Dewhurst, J. P., et al. (2008). Cluster observations of "crater" flux transfer events at the dayside high-latitude magnetopause. *Journal of Geophysical Research*, *113*, A07S04. https://doi.org/10.1029/2007JA012701

Paschmann, G., Haerendel, G., Papamastorakis, I., Sckopke, N., Bame, S. J., Gosling, J. T., & Russell, C. T. (1982). Plasma and magnetic field characteristics of magnetic flux transfer events. *Journal of Geophysical Research*, *87*(A4), 2159–2168. https://doi.org/10.1029/JA087iA04p02159

Paschmann, G., Papamastorakis, I., Baumjohann, W., Sckopke, N., Carlson, C. W., Sonnerup, B. U. Ö., & Lühr, H. (1986). The magneto-pause for large magnetic shear: AMPTE/IRM observations. *Journal of Geophysical Research*, *91*(A10), 11099. https://doi.org/10.1029/JA091ia10p11099

Phan, T. D., Drake, J. F., Shay, M. A., Mozer, F. S., & Eastwood, J. P. (2007). Evidence for an elongated (>60 ion skin depths) electron diffusion region during fast magnetic reconnection. *Physical Review Letters*, *99*(25), 255002. https://doi.org/10.1103/PhysRevLett.99.255002

Pritchett, P. L. (2008). Collisionless magnetic reconnection in an asymmetric current sheet. *Journal of Geophysical Research*, *113*(A6), A06210. https://doi.org/10.1029/2007JA012930

Pritchett, P. L., & Mozer, F. S. (2009). Asymmetric magnetic reconnection in the presence of a guide field. *Journal of Geophysical Research*, *114*, A11210. https://doi.org/10.1029/2009JA014343

Raeder, J. (2006). Flux transfer events: 1 Generation mechanism for strong southward IMF. *Annales Geophysicae*, *24*, 381–392. https://doi.org/10.5194/angeo-24-381-2006

Russell, C. T., & Elphic, R. C. (1978). Initial ISEE magnetometer results: Magnetopause observations. *Space Science Reviews*, *22*, 681–715. https://doi.org/10.1007/bf00212619

Russell, C. T., & Elphic, R. C. (1979). ISEE observations of flux transfer events at the dayside magnetopause. *Geophysical Research Letters*, *6*(1), 33–36. https://doi.org/10.1029/GL006i001p00033

Scholer, M. (1988). Strong core magnetic fields in magnetopause flux transfer events. *Geophysical Research Letters*, *15*(8), 748–751. https://doi.org/10.1029/GL015i008p00748

Shue, J.-H., Chao, J. K., Fu, H. C., Russell, C. T., Song, P., Khurana, K. K., & Singer, H. J. (1997). A new functional form to study the solar wind control of the magnetopause size and shape. *Journal of Geophysical Research*, *102*(A5), 9497–9511. https://doi.org/10.1029/97JA00196

Sibeck, D. G., Kuznetsova, M., Angelopoulos, V., Glassmeier, K.-H., & McFadden, J. P. (2008). Crater FTEs: Simulation results and THEMIS observations. *Geophysical Research Letters*, *35*, L17S06. https://doi.org/10.1029/2008GL033568

Sonnerup, B. U. Ö. (1979). Magnetic field reconnection. In C. F. Kennel, L. J. Lanzerotti, E. N. Parker (Eds.), *Solar system plasma physics* (Vol. 3, pp. 45–108). Amsterdam: North-Holland Pub.

Sonnerup, B. U. Ö., & Scheible, M. (1998). Minimum and maximum variance analysis. In G. Paschmann, & P. W. Daly (Eds.), *Analysis methods for multi-spacecraft data* (ISSI scientific report series SR-001) (pp. 185–220). Noordwiijk, The Netherlands: European Space Agency Publications Division.

Southwood, D. J., Saunders, M. A., Dunlop, M. W., Mier-Jedrzeiowicz, W. A. C., & Rijnbeek, R. P. (1986). A survey of flux transfer events recorded on the UKS spacecraft magnetometer. *Planetary and Space Science*, *34*(12), 1349–1359. https://doi.org/10.1016/0032-0633(86)90071-1

Stone, E., Frandsen, A., Mewaldt, R., Christian, E., Margolies, D., Ormes, J., & Snow, F. (1998). The Advanced Composition Explorer. *Space Science Reviews*, *86*(1/4), 1–22. https://doi.org/10.1023/A:1005082526237

Terasawa, T. (1983). Hall current effect on tearing mode instability. *Geophysical Research Letters*, *10*(6), 475–478. https://doi.org/10.1029/GL010i006p00475

Tóth, G., Chen, Y., Gombosi, T. I., Cassak, P., Markidis, S., & Peng, I. B. (2017). Scaling the ion inertial length and its implications for modeling reconnection in global simulations. *Journal of Geophysical Research: Space Physics*, *122*, 10,336–10,355. https://doi.org/10.1002/2017JA024189

Trottenberg, U., Oosterlee, C. W., & Schuller, A. (2000). *Multigrid*. San Diego: Academic Press. Hardcover ISBN 9780127010700

Wang, Y., Elphic, R. C., Lavraud, B., Taylor, M. G. G. T., Birn, J., Raeder, J., et al. (2005). Initial results of high-latitude magnetopause and low-latitude flank flux transfer events from 3 years of Cluster observations. *Journal of Geophysical Research*, *110*, A11221. https://doi.org/10.1029/2005JA011150

Wilder, F. D., Ergun, R. E., Eriksson, S., Phan, T. D., Burch, J. L., Ahmadi, N., et al. (2017). Multipoint measurements of the electron jet of symmetric magnetic reconnection with a moderate guide field. *Physical Review Letters*, *118*(26), 265101. https://doi.org/10.1103/PhysRevLett.118.265101

Zeiler, A., Biskamp, D., Drake, J. F., Rogers, B. N., Shay, M. A., & Scholer, M. (2002). Three-dimensional particle simulations of collisionless magnetic reconnection. *Journal of Geophysical Research*, *107*(A9), 1230. https://doi.org/10.1029/2001JA000287

Zhang, H., Kivelson, M. G., Khurana, K. K., McFadden, J., Walker, R. J., Angelopoulos, V., et al. (2010). Evidence that crater flux transfer events are initial stages of typical flux transfer events. *Journal of Geophysical Research*, *115*, A08229. https://doi.org/10.1029/2009JA015013